Chromo-dynamic multi-component lattice Boltzmann equation scheme for axial symmetry

SPENDLOVE, James Edward, XU, Xu <http://orcid.org/0000-0002-9721-9054>, SCHENKEL, Torsten, SEATON, Michael Andrew <http://orcid.org/0000-0002-4708-573X> and HALLIDAY, Ian <http://orcid.org/0000-0003-1840-6132>

Journal of Physics A: Mathematical and Theoretical

PAPER • **OPEN ACCESS**

Chromo-dynamic multi-component lattice Boltzmann equation scheme for axial symmetry

To cite this article: J Spendlove *et al* 2020 *J. Phys. A: Math. Theor.* **53** 145001

OPEN ACCESS
IOP Publishing
Journal of Physics A: Mathematical and Theoretical
J. Phys. A: Math. Theor. **53** (2020) 145001 (33pp)
https://doi.org/10.1088/1751-8121/ab777f

Chromo-dynamic multi-component lattice Boltzmann equation scheme for axial symmetry

J Spendlove[1], X Xu[1,2], T Schenkel[1,2], M Seaton[3] and I Halliday[1]

[1] Materials & Engineering Research Institute, Sheffield Hallam University, Howard Street, S1 1WB, United Kingdom
[2] Department of Engineering and Mathematics, Sheffield Hallam University, Howard Street, S1 1WB, United Kingdom
[3] Scientific Computing Department, UKRI STFC Daresbury Laboratory, Keckwick Lane, Warrington WA4 4AD, United Kingdom

E-mail: i.halliday@shu.ac.uk

Received 1 August 2019, revised 13 January 2020
Accepted for publication 18 February 2020
Published 18 March 2020

Abstract

We validate the chromo-dynamic multi-component lattice Boltzmann equation (MCLBE) simulation for immiscible fluids with a density contrast against analytical results for complex flow geometries, with particular emphasis on the fundamentals of the method, i.e. compliance with inter-facial boundary conditions of continuum hydrodynamics. To achieve the necessary regimes for the chosen validations, we develop, from a three-dimensional, axially-symmetric flow formulation, a novel, two-dimensional, pseudo Cartesian, MCLBE scheme. This requires the inclusion in lattice Boltzmann methodology of a continuously distributed source and a velocity-dependent force density (here, the metric force terms of the cylindrical Navier–Stokes equations). Specifically, we apply our model to the problem of flow past a spherical liquid drop in $\mathrm{Re} = 0$, $\mathrm{Ca} \to 0$ regime and, also, flow past a lightly deformed drop. The resulting simulation data, once corrected for the simulation's inter-facial micro-current (using a method we also advance herein, based on freezing the phase field) show good agreement with theory over a small range of density contrasts. In particular, our data extend verified compliance with the kinematic condition from flat (Burgin *et al* 2019 *Phys. Rev.* E **100** 043310) to the case of curved fluid–fluid interfaces. More generally, our results indicate a route to eliminate the influence of the inter-facial micro-current.

Keywords: lattice Boltzmann, multiphase flows, hydrodynamics

(Some figures may appear in colour only in the online journal)

1. Introduction

Since 1991, when Gunstensen and Rothman [1, 2] invented the technique, a range of increasingly sophisticated multi-component lattice Boltzmann (lB) equation variants have evolved. Still, Gunstensen and Rothman's method remains a milestone of statistical physics [3]. Current multi-component lattice Boltzmann equation (MCLBE) variants depart substantially from Gunstensen's. They may be classified by the physical content of their fluid–fluid interface algorithm. Broadly, where the kinetics of phase separation feature, *free-energy* methods [4, 5] and their thermodynamically consistent extensions, due to Wagner and co-workers [6–8], is a natural choice. In continuum, isothermal hydrodynamics, inter-facial fluid physics is defined by dynamic and kinematic conditions [10]. Here, MCLBE simulation may be performed using the phase field or, hereafter, chromo-dynamic method (which is a combination of the algorithms of Lishchuk *et al* [11] and d'Ortona *et al* [12]).

To induce fluid–fluid boundary effects, chromo-dynamic MCLBE uses an immersed boundary [13] (henceforth Lishchuk) force which requires appropriate corrections be applied to the velocity [14] and a computationally-efficient, analytic component segregation [12] (which is isotropic, mass-conserving and Galilean invariant). This synthesis is robust and transparent in its encapsulation of Laplacian interfacial tension and its no-traction condition [11]. It also has a very low micro-current which allows direct parametrization of inter-facial tension and width [15]. We note that Reiss and Phillips [16] developed inter-facial perturbation operators in place of the Lishchuk force which, arguably, offer the most consistent encapsulation of inter-facial tension in a kinetic-scale, distribution function-based technique. In its original form, chromo-dynamic MCLBE does not allow for a density contrast between immiscible fluids. Density-difference MCLBE methods of the chromo-dynamic class, based on multi-relaxation time (MRT) collision schemes, due to Ba *et al* [17], Liu *et al* [19], Wen *et al* [20] and Spendlove *et al* [21] have been developed and benchmarked, in applications such as the evolution of three-dimensional (3D) convective instabilities [17] and, recently, by careful comparisons with theoretical predictions in two-dimension (2D) with restricted symmetry [21, 24]. While this previous work certainly confirms the utility of the method, questions relating to its fundamental physical accuracy remain. Here, we aim to assess the extent to which 3D MCLBE simulation complies with the hydrodynamic boundary conditions of mutual impenetrability and the no-traction conditions using, note, comparison with appropriate analytic results for complex flow in the presence of non-uniform curvature. To achieve this, the noise introduced by the inter-facial micro-current and computability present significant difficulties. To overcome the influence of the inter-facial micro-current, we employ a phase-field freezing method, to overcome computational limitations we develop a pseudo-Cartesian methodology, which, itself, requires two extensions to lB to incorporate (i) spatially variable sources/sinks and (ii) velocity-dependent forces. The data we generate to validate boundary condition compliance implicitly supports our practical method for removing the influence of the inter-facial micro-current.

We organise this article as follows. In section 2 we outline chromo-dynamic MCLBE methodology, in section 3 we derive a pseudo Cartesian formulation suitable for our intended applications and develop a suitable MRT scheme, in section 4 we outline its application and in

section 5 we present and interpret our data. We conclude in section 6. Details of our analysis of the MRT scheme and high-order accurate lattice stencils are provided in appendices A and B respectively.

2. Background method

We express the chromo-dynamic variant in colour-blind form, designating immiscible fluid components red and blue, to be described by distribution functions $R_i(\mathbf{r},t)$ and $B_i(\mathbf{r},t)$ where:

$$f_i(\mathbf{r},t) = R_i(\mathbf{r},t) + B_i(\mathbf{r},t).$$

An MCLBE for immiscible fluids with a large density difference, based upon an MRT collision scheme for a fluid subject to an immersed boundary, or body force, $F_\alpha(\mathbf{r})$ may be formulated as follows:

$$f_i(\mathbf{r}+\delta_t\mathbf{c}_i, t+\delta_t) = f_i(\mathbf{r},t) - \sum_{j=0}^{Q-1} A_{ij}(f_j(\mathbf{r},t) - f_j^{(0)}(\rho,\mathbf{v})) + F_{1i} + F_{2i} + F_{3i}, \tag{1}$$

where the density-difference supporting equilibrium, $f_i^{(0)}(\rho,\mathbf{v})$, redistributes mass away from the rest ($i=0$) link via term ϕ_i:

$$f_i^{(0)}(\rho,\mathbf{v}) = \rho\phi_i + t_i\rho\left(\frac{v_\alpha c_{i\alpha}}{c_s^2} + \frac{v_\alpha v_\beta c_{i\alpha}c_{i\beta}}{2c_s^4} - \frac{v^2}{2c_s^2}\right). \tag{2}$$

In equation (1), A_{ij} is an element of the collision matrix and source terms F_{1i},..,F_{3i} correct the dynamics for large density contrasts, external body force densities, D_α, and flow sources/sinks respectively. In section 3, we find appropriate forms for F_{1i},..,F_{3i}. We return to parameter ϕ_i shortly.

An external force density D_α is, in general, a sum of distinct contributions. We shall be concerned, here, with velocity-dependent forces which we expose by writing:

$$D_\alpha = G_\alpha(\mathbf{r}) + F_\alpha(\mathbf{r},\mathbf{v}),$$

in which $\mathbf{G}$ might represent e.g. gravity, or the Lishchuk force (see equation (8) below). This separation is motivated by the definition of force-adjusted macroscopic observables:

$$\begin{aligned} &\rho_R(\mathbf{r},t) = \sum_i R_i(\mathbf{r},t), \quad \rho_B(\mathbf{r},t) = \sum_i B_i(\mathbf{r},t) \\ &\mathbf{v} = \frac{\sum_i f_i(\mathbf{r},t)\mathbf{c}_i}{\rho} + \frac{\mathbf{D}}{2\rho}. \end{aligned} \tag{3}$$

Apparently, when a contribution to $\mathbf{D}$ depends upon velocity $\mathbf{v}$, equation (3) will define an implicit problem to be solved for $\mathbf{v}$. Above, ρ, ρ_R, ρ_B, i, δ_t, $c_{i\alpha}$, t_i and c_s denote overall nodal density, red fluid nodal density, blue fluid nodal density, link-index, time step, the α component of the ith lattice basis vector, the weight for link i and the colour-blind speed of sound (second order tensor lattice isotropy constant). A significant part of our methodology will be to develop explicit solutions for the third of equation (3) for $\mathbf{v}$, when $F_\alpha(\mathbf{v})$ depends upon spatial velocity gradients. In implementation, many quantities in equations (20), (21) and (8) will clearly require the numerical computation of gradients, as described below.

Returning to the mass activation parameter now:

$$\phi_i = \begin{cases} \frac{\alpha_R \rho_R}{\rho} + \frac{\alpha_B \rho_B}{\rho}, & i = 0, \\ kt_i \left[(1-\alpha_R)\frac{\rho_R}{\rho} + (1-\alpha_B)\frac{\rho_B}{\rho} \right], & i \neq 0, \end{cases} \tag{4}$$

where α_R and α_B are chosen to control the fluids' contrast in density:

$$\Lambda \equiv \frac{\rho_{0R}}{\rho_{0B}} = \frac{c_{sB}^2}{c_{sR}^2} = \frac{1-\alpha_B}{1-\alpha_R}, \tag{5}$$

and, for D2Q9, $k = \frac{9}{5}$ [24]. In equation (5), ρ_{0C} is the density deep within the coloured component $C = R, B$ and the third part of the equality reflects mechanical stability of a flat interface. The speed of sound in the red (blue) component is therefore $c_{sR} = \kappa\sqrt{1-\alpha_R}$ ($c_{sB} = \kappa\sqrt{1-\alpha_B}$) with κ a constant. We find κ by noting that $\alpha_R \to \alpha_B$ implies $\Lambda \to 1$; however, considering equations (2) and (4), we see the traditional equilibrium [18] is recovered for $\alpha_R = \alpha_B = \frac{4}{9}$: in the latter, the speed of sound (in lattice units, in D2Q9) is $\frac{1}{\sqrt{3}}$, hence $\frac{1}{3} = \kappa^2\left(1 - \frac{4}{9}\right)$, which gives $\kappa = \sqrt{\frac{3}{5}}$ and hence $c_{sC} = \sqrt{\frac{3(1-\alpha_C)}{5}}$. Accordingly, the pressure step across the interface of a red drop suspended in a blue fluid is:

$$\Delta p = \frac{3}{5}\left[(1-\alpha_R)\rho_R - (1-\alpha_B)\rho_B\right]. \tag{6}$$

Immiscible species are identified in simulation by a generalised colour index, or phase field [17]:

$$\rho^N \equiv \left(\frac{\rho_R}{\rho_{0R}} - \frac{\rho_B}{\rho_{0B}}\right) / \left(\frac{\rho_R}{\rho_{0R}} + \frac{\rho_B}{\rho_{0B}}\right), \tag{7}$$

in terms of which the Lishchuk force, $\mathbf{G}$ (which carries inter-facial tension effects [11]) is:

$$\mathbf{G} = \frac{1}{2}\sigma K \nabla \rho^N, \quad K = -\underline{\nabla} \cdot \hat{n}, \quad \hat{n} = \frac{\nabla \rho^N}{|\nabla \rho^N|}. \tag{8}$$

Here, σ is the surface tension parameter and K the interface's mean curvature. ρ^N is considered to be continuous: $\rho^N \in [-1, 1]$ with $\rho^N = 1(-1)$ indicative of pure red (blue) fluid and changes occur rapidly in the inter-facial region. Since it identifies the fluid component, the value of index ρ^N may be used to control the value of e.g. kinematic viscosity, by introducing into collision matrix eigenvalue λ_3 an appropriate functional dependence upon ρ^N:

$$\nu(\rho^N) = \frac{1}{6}\left(\frac{2}{\lambda_3(\rho^N)} - 1\right).$$

The functional form of $\lambda_3(\rho^N)$ has been shown to have significant consequences [22, 23].

Kinetic-scale, post-collision colour species segregation, or re-allocation, is an adaptation of the method of d'Ortona *et al* [12] , which may be written as:

$$C_i^{++}(\mathbf{r}, t) = \frac{\rho_C(\mathbf{r}, t)}{\rho(\mathbf{r}, t)} f_i(\mathbf{r}, t)^+ \pm \beta \frac{\phi_i(\mathbf{r}, t)\rho_R(\mathbf{r}, t)\rho_B(\mathbf{r}, t)}{\rho(\mathbf{r}, t)} \hat{\mathbf{n}} \cdot \delta_t \hat{\mathbf{c}}_i, \tag{9}$$

where superscript $+$ $(++)$ denotes a post-collision (post re-colour) quantity, β is a chosen segregation parameter [12] and the $+$ $(-)$ sign is used for the red (blue) component. We note

that this segregation rule is mass-conserving, simple to implement, local (given a constant director, $\hat{\mathbf{n}}$) and perhaps most significantly, 'bottom-up', i.e. a kinetic scale postulate which is justified *a posteriori*. Indeed, it has recently been shown that equation (9) is consistent with the following continuum-scale kinematics (expressed relative to the red component) [24], for uniform fluid motion:

$$\begin{aligned}
&\frac{\partial \rho_R}{\partial t} + \frac{1}{2}\delta_t^2 \frac{\partial^2 \rho_R}{\partial t^2} + v_\gamma \partial_\gamma \rho_R \\
&= \frac{k}{2} c_s^2 (1-\alpha_R)\delta_t \nabla^2 \left(\frac{\rho_R^2}{\rho} \right) \\
&+ \frac{k}{2} c_s^2 (1-\alpha_B)\delta_t \nabla^2 \left(\frac{\rho_R \rho_B}{\rho} \right) \\
&+ \frac{1}{2}\delta_t v_\alpha v_\beta \partial_\alpha \partial_\beta \rho_R \\
&- \delta_t \beta (1-\alpha_R) k c_s^2 n_\gamma \partial_\gamma \left(\frac{\rho_R^2 \rho_B}{\rho^2} \right) \\
&- \delta_t \beta (1-\alpha_B) k c_s^2 n_\gamma \partial_\gamma \left(\frac{\rho_R \rho_B^2}{\rho^2} \right) \\
&+ 2\delta_t c_s^4 \partial_\alpha \partial_\beta \left(\frac{\rho_R F_{\alpha\beta}}{\rho} \right).
\end{aligned} \tag{10}$$

In the above, the last term on the right hand side originates in the dynamics correction term, F_{1i} (see equation (20)) and determines the effect on the model kinematics of the dynamics [24]. When the term $2\delta_t c_s^4 \partial_\alpha \partial_\beta \left(\frac{\rho_R F_{\alpha\beta}}{\rho} \right)$ in equation (10) is small, Burgin *et al* [24] find the following, physically correct chromo-dynamics, obtained by solving equation (10):

$$\rho_R(\mathbf{r}, t) = \frac{\rho_{0R}}{2}\big(1 + \tanh(\beta \hat{\mathbf{n}} \cdot (\mathbf{r} - \mathbf{v}t)\big),$$

with equivalent behaviour for the blue component. This result represents interface advection within fluids moving at uniform velocity. Note that, with this solution, the corresponding colour field profile is amenable to numerical differentiation i.e. $\rho^N(\mathbf{r}, t) \to \tanh\left[\beta \hat{\mathbf{n}} \cdot (\mathbf{r} - \mathbf{v}t)\right]$, so that the chromo-dynamic field is approximately a material invariant at order δ_t^2. On the other hand, the error term in equation (10) constitutes an issue even with pure advection, i.e. it is present even in uniform flow, which is shown to restrict applicability of the method according to approximate relation $\Lambda u = \text{constant}$ [24]. Taking the order δ_t approximation in equation (10), $\frac{D\rho_C}{Dt} \approx 0$ equivalent, Burgin *et al* [24] arrive at the following, at lowest order of Chapman–Enskog theory:

$$\frac{D\rho_C}{Dt_0} = 0, \quad C \in [R, B], \tag{11}$$

for both fluid components. The above result will be seen to be central when deriving our pseudo Cartesian, chromo-dynamic MCLBE MRT scheme, in section 3.

3. MRT scheme for axi-symmetric chromo-dynamic MCLBE

With the overall aim of facilitating the efficient benchmarking of multi-component flows with axial symmetry, we first develop a quasi-two-dimensional (2D), Cartesian representation,

from continuum fluid dynamics. The resulting formulation motivates two, essentially distinct, developments to lB methodology. First, a MCLBE MRT scheme (for a system with density contrast) able to handle spatially distributed flow sources/sinks and second, an advance to the methodology for incorporating velocity-dependent forces in MCLBE. We therefore establish a pseudo 2D representation of 3D, axially symmetric flows, then develop a suitable MCLBE scheme after Dellar *et al* and finally extend to velocity-dependent forces.

3.1. Two-dimensional representation of axially symmetric flows

Figure 1 illustrates the reduction from three to two dimensions, of a multi-component system with axial symmetry. A pseudo 2D system may be derived by discounting ignorable cylindrical polar co-ordinate ϕ, with an equivalent Cartesian equivalent system (x, z) parametrizing the $\phi = 0$ plane. The Navier–Stokes and continuity equations for incompressible flow, expressed in cylindrical polar co-ordinates, are [10]:

$$\begin{aligned}&\frac{\partial v_r}{\partial t} + v_r\frac{\partial v_r}{\partial r} + \frac{v_\phi}{r}\frac{\partial v_r}{\partial \phi} + v_z\frac{\partial v_r}{\partial z} - \frac{v_\phi^2}{r}\\ &= -\frac{1}{\rho}\frac{\partial p}{\partial r} + \frac{\eta}{\rho}\left[\frac{1}{r}\frac{\partial}{\partial r}\left(r\frac{\partial v_r}{\partial r}\right) + \frac{1}{r^2}\frac{\partial^2 v_r}{\partial \phi^2} + \frac{\partial^2 v_r}{\partial z^2} - \frac{2}{r^2}\frac{\partial v_\phi}{\partial \phi} - \frac{v_r}{r^2}\right],\end{aligned} \tag{12}$$

$$\begin{aligned}&\frac{\partial v_\phi}{\partial t} + v_r\frac{\partial v_\phi}{\partial r} + \frac{v_\phi}{r}\frac{\partial v_\phi}{\partial \phi} + v_z\frac{\partial v_\phi}{\partial z} + \frac{v_r v_\phi}{r}\\ &= -\frac{1}{\rho r}\frac{\partial p}{\partial \phi} + \frac{\eta}{\rho}\left[\frac{1}{r}\frac{\partial}{\partial r}\left(r\frac{\partial v_\phi}{\partial r}\right) + \frac{1}{r^2}\frac{\partial^2 v_\phi}{\partial \phi^2} + \frac{\partial^2 v_\phi}{\partial z^2} + \frac{2}{r^2}\frac{\partial v_r}{\partial \phi} - \frac{v_\phi}{r^2}\right],\end{aligned} \tag{13}$$

$$\begin{aligned}&\frac{\partial v_z}{\partial t} + v_r\frac{\partial v_z}{\partial r} + \frac{v_\phi}{r}\frac{\partial v_z}{\partial \phi} + v_z\frac{\partial v_z}{\partial z}\\ &= -\frac{1}{\rho}\frac{\partial p}{\partial z} + \frac{\eta}{\rho}\left[\frac{1}{r}\frac{\partial}{\partial r}\left(r\frac{\partial v_z}{\partial r}\right) + \frac{1}{r^2}\frac{\partial^2 v_z}{\partial \phi^2} + \frac{\partial^2 v_z}{\partial z^2}\right],\end{aligned} \tag{14}$$

$$\frac{1}{r}\frac{\partial}{\partial r}(r v_r) + \frac{1}{r}\frac{\partial v_\phi}{\partial \phi} + \frac{\partial v_z}{\partial z} = 0. \tag{15}$$

In axial-symmetry, with the following replacements:

$$r \longrightarrow x, \quad v_r \to v_x, \tag{16}$$

this system reduces to a 2D, quasi-Cartesian form wherein metric terms of the acceleration equations transform to velocity-dependent accelerations and the continuity equation acquires a source:

$$\begin{aligned}\frac{\partial v_\alpha}{\partial t} + (\mathbf{v}\cdot\nabla)\, v_\alpha &= -\frac{1}{\rho}\frac{\partial p}{\partial x_\alpha} + \frac{\eta}{\rho}\nabla^2 v_\alpha + a_\alpha, \quad \alpha = x, z\\ \frac{\partial v_x}{\partial x} + \frac{\partial v_z}{\partial z} &= A.\end{aligned}$$

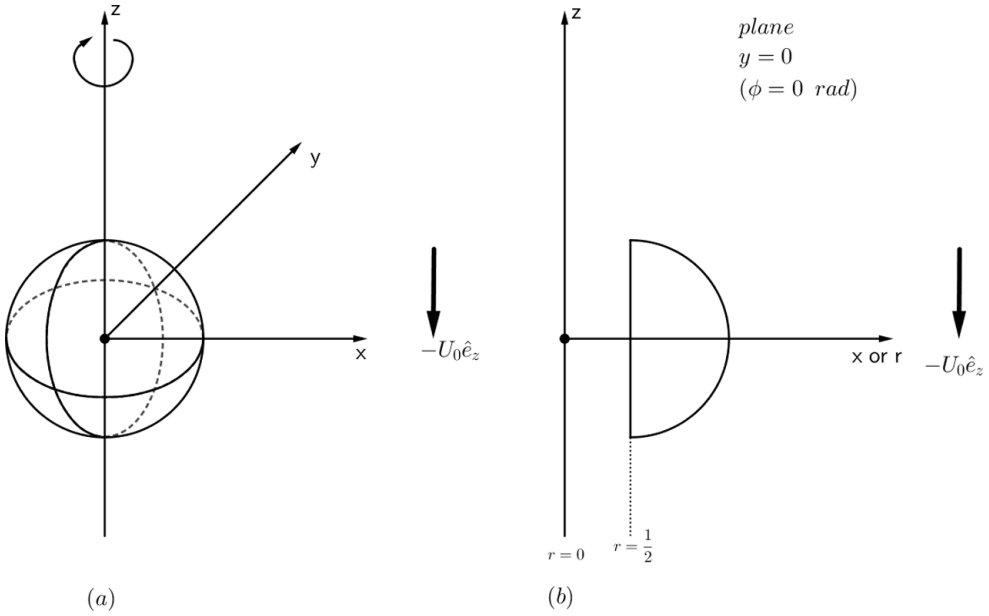

Figure 1. Schematic illustrating the reduction from 3D to 2D, for our multi-component drop system with the corresponding computational domain, used in simulation. Asterisks identify discrete, lattice quantities. Diagrams are not to scale. In (a) the sphere represents a liquid drop of radius R. The 2D system in (b) is described using cylindrical polar co-ordinates (r, z), i.e. ϕ is ignorable. Cartesian equivalent system (x, z) parameterizes the $\phi = 0$ plane. Our domain is part of the region $x \in [0.5, \infty)$, $z \in (-\infty, \infty)$, i.e. the symmetry boundary $r = 0$ lies outside simulations. Boundaries are implemented straightforwardly, to achieve the following: (i) an origin of lattice co-ordinate $x^* = 0$ corresponding to $x = \frac{1}{2}$ containing the effect of an axis of symmetry at $x = 0$, (ii) at large $|z^*|$, periodic replicas of the system and (iii) at large x^* mid-link bounce-back, to represent a no-slip boundary located at large x.

Above, $\nabla = \left(\frac{\partial}{\partial x}, \frac{\partial}{\partial z}\right)$ and $\mathbf{a}$ (A) denotes an acceleration (source/sink):

$$a_x = \frac{\eta}{\rho}\left(\frac{1}{x}\frac{\partial v_x}{\partial x} - \frac{v_x}{x^2}\right), \quad a_z = \frac{\eta}{\rho}\frac{1}{x}\frac{\partial v_z}{\partial x}, \quad A = -\frac{v_x}{x}. \tag{17}$$

After straightforward algebra, an equivalent velocity-dependent body force density (with units of N m^{-3}) and continuity source may be identified for the weakly compressible formulation characteristic of lattice Boltzmann:

$$\begin{aligned} F_x(\mathbf{v}) &= \eta\frac{\partial}{\partial x}\left(\frac{v_x}{x}\right), \quad F_z(\mathbf{v}) = \frac{\eta}{x}\frac{\partial v_z}{\partial x}, \\ A(\mathbf{v}) &= -\rho\left(\frac{v_x}{x}\right). \end{aligned} \tag{18}$$

Since we occupy the $\phi = 0$ plane of a cylindrical polar co-ordinate system with axial symmetry, the Mean curvature in equation (8), for the Lishchuk force, should, however, be computed using the cylindrical polar divergence:

$$K = -\underline{\nabla}\cdot\hat{n} = -\frac{\partial\hat{n}_x}{\partial x} - \frac{\partial\hat{n}_z}{\partial z} - \frac{\hat{n}_x}{x}. \tag{19}$$

Clearly equations (18) and (19) contain spatial gradients. In simulation, such gradients are computed using stencils based upon lattice link vectors, $\mathbf{c}_i$. For example, by exploiting lattice tensor isotropy it is possible to devise a compact, third-order stencil : $\frac{\partial f}{\partial x_\alpha} \approx 3\sum_i t_i f(\mathbf{r}+\delta_t\mathbf{c}_i)c_{i\alpha}$, where f denotes the scalar function to be differentiated and δ_t is the simulation time step. In appendix B we derive the high order stencils necessary in part of this work.

The continuity equation source/sink, A, introduced above, may be understood in terms of the system's geometry. Consider an annular volume element with volume $\mathrm{d}r\mathrm{d}z(r\mathrm{d}\phi)$. With $v_r =$ constant and $\rho =$ constant, there still exists a mass flux differential between the volume element's curved exterior and interior surfaces, the relevant fluxes being $\rho v_r(r+\mathrm{d}r)\mathrm{d}\phi\mathrm{d}z$ and $\rho v_r r\mathrm{d}\phi\mathrm{d}z$, respectively. The difference in mass flux is equivalent to a source or sink per unit volume of the 2D, pseudo Cartesian domain:

$$\frac{\rho v_r r\mathrm{d}\phi\mathrm{d}z - \rho v_r(r+\mathrm{d}r)\mathrm{d}\phi\mathrm{d}z}{r\mathrm{d}\phi\mathrm{d}z} = -\frac{\rho v_r}{r} \to A(\mathbf{v}).$$

Henceforth, we denote by (x^*, z^*) the discrete lattice co-ordinate corresponding to (x, z) respectively.

3.2. MRT scheme

From section 3.1, we see a quasi-Cartesian lB model for axi-symmetric flow must encompass velocity dependent forces and sources. Here, we derive a MRT scheme using the method of Dellar, able to incorporate geometrical forces, $\mathbf{F}(\mathbf{v})$ and sources, A, alongside other simpler body forces, $\mathbf{G}$ and also to treat immiscible fluids with a density contrast, Λ.

Dellar developed the most logically consistent approach to an MRT scheme for single component flow [25]. It avoids explicit assignment of collision matrix elements, A_{ij}. The collision matrix is, instead, implicitly defined by its eigenvalues and eigenvectors, a majority being assigned naturally in the Chapman–Enskog process. By a Chapman–Enskog analysis of the kinetic equation (1), using the framework of Guo *et al* [14], we derive, in appendix A, an MRT scheme-based collision model. Our analysis is performed in $D2Q9$ with the lattice link vectors $\mathbf{c}_i$ and indexing defined in figure 2. The scheme is derived colour-blind, so as to clarify the coupling between it and the model kinematics [24]. Put another way, we wish to incorporate the effects of the chromo-dynamics MCLBE segregation or re-colour step in the macroscopic description. Based on an analysis of the f_i, we demonstrate correct macroscopic dynamics for the following kinetic sources:

$$F_{1i} = t_i(c_{i\alpha}c_{i\beta} - c_s^2\delta_{\alpha\beta})F_{\alpha\beta}(\rho_R, \rho_B, \rho^N, \Lambda, \mathbf{v}), \tag{20}$$

$$F_{2i} = t_i\left[\frac{D_\alpha c_{i\alpha}}{c_s^2} + \frac{1}{2c_s^4}\left(1-\frac{\lambda_3}{2}\right)\times(D_\alpha u_\beta - D_\beta u_\alpha)(c_{i\alpha}c_{i\beta} - c_s^2\delta_{\alpha\beta})\right], \tag{21}$$

$$F_{3i} = t_i A - \left(1-\frac{\lambda_3}{2}\right)Au_\alpha u_\beta - \frac{1}{3}A\delta_{\alpha\beta}. \tag{22}$$

Above, λ_3 is an eigenvalue of matrix $\mathbf{A}$, which determines the kinematic viscosity of the lattice fluid, the tensor:

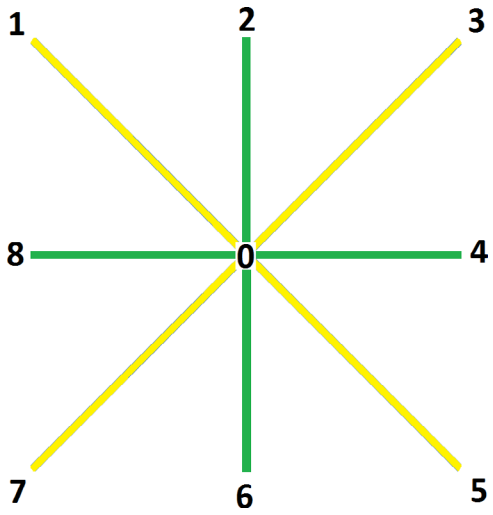

Figure 2. Schematic of a square lattice in D2Q9 with the indexing convention used throughout. Note that even (odd) value of link index i label short (long) links.

$$F_{\alpha\beta} = \frac{t_i}{2c_s^4}\left(1 - \frac{\lambda_3}{2}\right) \times \left\{\frac{1}{3}\rho\partial_\gamma u_\gamma \delta_{\alpha\beta} - (u_\alpha \partial_\beta \Phi' + u_\beta \partial_\alpha \Phi' + u_\gamma \partial_\gamma \Phi' \delta_{\alpha\beta})\right\},$$

and

$$\Phi' = \frac{3}{5}(1 - \alpha_R)(\rho_R + \Lambda\rho_B) - \frac{1}{3}\rho. \tag{23}$$

Clearly, to use equations (1), (20), (21) and (23) to evolve the f_i requires the elements of **A**. To avoid this expense, we follow Dellar's approach and use a complete set of linearly-independent macro-scopic modes, $m^{(p)}$, $p = 0, 1, .., (Q-1)$, defined in table 1. A majority of these are physical i.e. $m^{(p)} = \sum_i h_i^{(p)} f_i$ represent observables like momentum. However, for closure, a subset of 'ghost modes' require a second lattice link weight function, g_i:

$$g_i = \begin{cases} 0 & i = 0 \\ 4 & i = \text{ odd} \\ -2 & i = \text{ even} \end{cases}$$

where, e.g. the designation 'odd' indicates a long lattice link, indexed by an odd value of subscript i (see figure 2) Conveniently, the $m^{(p)}$ turn out to obey scalar relaxation equations, the parameters for which, we will show, effectively define the elements of **A**.

We define a projection matrix, comprised of linearly independent left row collision matrix eigenvectors, $\mathbf{h}^{(p)}$, each the projector of a mode, $m^{(p)}$:

$$\mathbf{M} \equiv \left(\mathbf{h}^{(0)}, \mathbf{h}^{(1)}, \cdots, \mathbf{h}^{(8)}\right)^T,$$

such that

Table 1. Collision matrix eigenspectrum. Left row eigenvectors (projectors), $\mathbf{h}^{(p)}, p \in [0,8]$, corresponding eigenvalues, corresponding physical significance (if any) and corresponding equilibria for mode $m^{(p)} \equiv \sum_i h_i^{(p)} f_i$ of the collision matrix, $\mathbf{A}$.

Eigenvector	Component	Definition	Eigenvalue, λ_p	mode, $m^{(p)}$	Physical interpretation	Equilibrium
$\mathbf{h}^{(0)}$	$h_i^{(0)}$	1_i	0	ρ	Density	ρ
$\mathbf{h}^{(1)}$	$h_i^{(1)}$	c_{ix}	0	ρu_x	x momentum	ρu_x
$\mathbf{h}^{(2)}$	$h_i^{(2)}$	c_{iy}	0	ρu_y	y momentum	ρu_y
$\mathbf{h}^{(3)}$	$h_i^{(3)}$	c_{ix}^2	λ_3	P_{xx}	See equation (A.2)	$\Pi_{xx}^{(0)}$
$\mathbf{h}^{(4)}$	$h_i^{(4)}$	c_{iy}^2	λ_3	P_{yy}	See equation (A.2)	$\Pi_{yy}^{(0)}$
$\mathbf{h}^{(5)}$	$h_i^{(5)}$	$c_{ix}c_{iy}$	λ_3	P_{xy}	See equation (A.2)	$\Pi_{xy}^{(0)}$
$\mathbf{h}^{(6)}$	$h_i^{(6)}$	g_i	λ_6	N	—	0
$\mathbf{h}^{(7)}$	$h_i^{(7)}$	$g_i c_{ix}$	λ_7	J_x	—	0
$\mathbf{h}^{(8)}$	$h_i^{(8)}$	$g_i c_{iy}$	λ_7	J_y	—	0

$$\left(m^{(0)}, m^{(1)}, ..., m^{(8)}\right)^T = (\rho, \rho u_x, \rho u_y, \sigma_{xx}, \sigma_{yy}, \sigma_{xy}, N, J_x, J_y)^T = \mathbf{M}\mathbf{f}, \tag{24}$$

(see table 1). Above, the column vector $\mathbf{f} \equiv (f_0, f_1, ..., f_8)^T$ and $\mathbf{M}$ is a column vector, each element of which is a left eigenvector. We define *all* the $\mathbf{h}^{(p)}$ as polynomial expressions in the lattice basis. Let us project evolution equation (1) using left multiplication by $\mathbf{M}$:

$$\mathbf{M}\,\mathbf{f}^{+} = \mathbf{M}\,\mathbf{f} + \mathbf{M}\,\mathbf{A}\,\mathbf{M}^{-1}\left(\mathbf{M}\,\mathbf{f}^{(0)} - \mathbf{M}\,\mathbf{f}\right) + \mathbf{M}\,\mathbf{F}, \tag{25}$$

where $\mathbf{F}$ is the column vector whose elements are the source terms, $F_i = F_{1i} + F_{2i} + F_{3i}$, in the evolution equation (1), i.e. $\mathbf{F} \equiv (F_0, F_1, ..., F_8)^T$. Using equation (24), the above projected evolution equation decomposes into a set of forced scalar relaxation equations, one for each mode:

$$\begin{aligned} m^{(p)+} &= m^{(p)} + \lambda_p\left(m^{(0)(p)} - m^{(p)}\right) + S^{(p)}, \\ S^{(p)} &= \sum_{j=0}^{8} M_{pj} F_j, \quad p = 0, 1, ..., (Q-1), \\ m^{(0)(p)} &= \sum_{j=0}^{8} M_{pj} f_j^{(0)}, \quad p = 0, 1, ..., (Q-1). \end{aligned} \tag{26}$$

In equation (25) it is immediate from the properties of the $\mathbf{h}^{(p)}$ that $\mathbf{\Lambda} = \mathbf{M}\,\mathbf{A}\,\mathbf{M}^{-1}$, with $\mathbf{\Lambda} \equiv \text{ diag}(\lambda_0,\ \lambda_1, ..., \lambda_8)$, whence we obtain the stated set of scalar, modal relaxation equations. Note that zero eigenvalues are associated with physical modes subject to conservation principles. The problem of developing an MRT scheme now reduces to one of computing

appropriate equilibria, $m^{(0)(p)}$, and source terms $S^{(p)}$. These computations are straightforward when performed within the framework of Guo *et al*, [14]. In appendix A, we use these authors' approach to write our kinetic equation source $(F_{1i} + F_{2i} + F_{3i})$ in terms of the following tensor:

$$\begin{aligned} C_{\alpha\beta} = &\left(1 - \frac{\lambda_3}{2}\right)\left[u_\alpha\left(F_\beta - \partial_\beta\Phi'\right) + u_\beta\left(F_\alpha - \partial_\alpha\Phi'\right)\right] \\ &- \left(1 - \frac{\lambda_3}{2}\right)\left[u_\gamma\partial_\gamma\Phi' - \frac{1}{3}\rho\partial_\gamma u_\gamma\right]\delta_{\alpha\beta} \\ &- \left(1 - \frac{\lambda_3}{2}\right)Au_\alpha u_\beta - \frac{A}{3}\delta_{\alpha\beta}. \end{aligned} \tag{27}$$

Then, in terms of $C_{\alpha\beta}$, above, we have:

$$\begin{aligned} S^{(0)} &= \mathbf{h}^{(0)}\cdot\mathbf{F} = \sum_i h_i^{(0)}F_i = A, \\ S^{(1)} &= \mathbf{h}^{(1)}\cdot\mathbf{F} = \sum_i h_i^{(1)}F_i = \sum_i c_{ix}F_i = nF_x\delta_t, \\ S^{(2)} &= \mathbf{h}^{(2)}\cdot\mathbf{F} = \sum_i h_i^{(2)}F_i = \sum_i c_{iy}F_i = nF_y\delta_t, \\ S^{(3)} &= \mathbf{h}^{(3)}\cdot\mathbf{F} = \sum_i h_i^{(3)}F_i = \sum_i c_{ix}^2F_i = C_{xx} + \frac{A}{3}, \\ S^{(4)} &= \mathbf{h}^{(4)}\cdot\mathbf{F} = \sum_i h_i^{(4)}F_i = \sum_i c_{iy}^2F_i = C_{yy} + \frac{A}{3}, \\ S^{(5)} &= \mathbf{h}^{(5)}\cdot\mathbf{F} = \sum_i h_i^{(5)}F_i = \sum_i c_{ix}c_{iy}F_i = \frac{1}{2}(C_{xy} + C_{yx}), \\ S^{(6)} &= \mathbf{h}^{(6)}\cdot\mathbf{F} = \sum_i h_i^{(6)}F_i = \sum_i g_iF_i = 0, \\ S^{(7)} &= \mathbf{h}^{(7)}\cdot\mathbf{F} = \sum_i h_i^{(7)}F_i = \sum_i g_ic_{ix}F_i = 0, \\ S^{(8)} &= \mathbf{h}^{(8)}\cdot\mathbf{F} = \sum_i h_i^{(8)}F_i = \sum_i g_ic_{iy}F_i = 0. \end{aligned}$$

We note that the source term F_i has no projection onto the non-hydrodynamic modes N, J_x, J_y. For the modal projections of the particle distribution function equilibrium, $f_i^{(0)}(\rho, \mathbf{v})$, we have:

$$\mathbf{h}^{(0)}\cdot\mathbf{f}^{(0)}=\sum_i h_i^{(0)}f_i^{(0)}=\sum_i 1_i f_i^{(0)}=\rho,$$
$$\mathbf{h}^{(1)}\cdot\mathbf{f}^{(0)}=\sum_i h_i^{(1)}f_i^{(0)}=\sum_i c_{ix}f_i^{(0)}=\rho u_x,$$
$$\mathbf{h}^{(2)}\cdot\mathbf{f}^{(0)}=\sum_i h_i^{(2)}f_i^{(0)}=\sum_i c_{iy}f_i^{(0)}=\rho u_y,$$
$$\mathbf{h}^{(3)}\cdot\mathbf{f}^{(0)}=\sum_i h_i^{(3)}f_i^{(0)}=\sum_i c_{ix}^2 f_i^{(0)}=\Pi_{xx}^{(0)}$$
$$\mathbf{h}^{(4)}\cdot\mathbf{f}^{(0)}=\sum_i h_i^{(4)}f_i^{(0)}=\sum_i c_{iy}^2 f_i^{(0)}=\Pi_{yy}^{(0)},$$
$$\mathbf{h}^{(5)}\cdot\mathbf{f}^{(0)}=\sum_i h_i^{(5)}f_i^{(0)}=\sum_i c_{ix}c_{iy}f_i^{(0)}=\Pi_{xy}^{(0)},$$
$$\mathbf{h}^{(6)}\cdot\mathbf{f}^{(0)}=\sum_i h_i^{(6)}f_i^{(0)}=\sum_i g_i f_i^{(0)}=\frac{9}{5}\alpha_R\rho_R+\frac{9}{5}\alpha_B\rho_B-\frac{4}{5}\rho,$$
$$\mathbf{h}^{(7)}\cdot\mathbf{f}^{(0)}=\sum_i h_i^{(7)}f_i^{(0)}=\sum_i g_i c_{ix}f_i^{(0)}=0,$$
$$\mathbf{h}^{(8)}\cdot\mathbf{f}^{(0)}=\sum_i h_i^{(8)}f_i^{(0)}=\sum_i g_i c_{iy}f_i^{(0)}=0.$$

With sources and equilibria defined, it is possible to write down the full set of modal evolution equations. These are stated for all the $Q=9$ modes ρ, (ρu_x), (ρu_y), P_{xx}, P_{yy}, P_{xy}, N, J_x and J_y in appendix A.

An inversion, from mode space, directly to obtain the post-collision distribution function may be performed:

$$\mathbf{f}^{+}=\mathbf{M}^{-1}\,\mathbf{m}^{+}. \tag{28}$$

Here, a distinct advantage of Dellar's approach is that projection matrix $\mathbf{M}$ may be inverted based upon lattice isotropies. Define the components of column vectors $\mathbf{k}^{(p)}$, $p=0,1,..,8$ as follows:

$$k_i^{(0)}=2t_i-\frac{3}{2}t_i\left(c_{ix}^2+c_{iy}^2\right),$$
$$k_i^{(1)}=3t_i c_{ix},$$
$$k_i^{(2)}=3t_i c_{iy},$$
$$k_i^{(3)}=\frac{9}{2}t_i c_{ix}^2-\frac{3}{2}t_i,$$
$$k_i^{(4)}=\frac{9}{2}t_i c_{iy}^2-\frac{3}{2}t_i,$$
$$k_i^{(5)}=9t_i c_{ix}c_{iy},$$
$$k_i^{(6)}=\frac{1}{4}g_i t_i,$$
$$k_i^{(7)}=\frac{3}{8}g_i t_i c_{ix},$$
$$k_i^{(8)}=\frac{3}{8}g_i t_i c_{iy},$$

It is straightforward, using the usual lB simulation lattice properties of isotropy of even tensors (see e.g. equations (A.3)–(A.5)), to show that $\mathbf{h}^{(p)} \cdot \mathbf{k}^{(p')} = \delta_{pp'}$ and hence it follows:

$$\mathbf{M}^{-1} = \left(\mathbf{k}^{(0)}, \mathbf{k}^{(1)}, \cdots, \mathbf{k}^{(8)}\right), \tag{29}$$

whence, using equation (28):

$$\begin{aligned} f_i^+ &= (M)_{ij}^{-1}\, m_j^+ \\ &= t_i \Bigg\{ \left[2 - \frac{3}{2}\left(c_{ix}^2 + c_{iy}^2\right)\right]\rho^+ \\ &\quad + 3\left((\rho u_x)^+ c_{ix} + (\rho u_y)^+ c_{iy}\right) \\ &\quad + \frac{9}{2}\left(P_{xx}^+ c_{ix}^2 + 2P_{xy}^+ c_{ix}c_{iy} + P_{yy}^+ c_{iy}^2\right) \\ &\quad - \frac{3}{2}\left(P_{xx}^+ + P_{yy}^+\right) \\ &\quad + \frac{1}{4} g_i N^+ + \frac{3}{8} g_i \left(J_x^+ c_{ix} + J_y^+ c_{iy}\right) \Bigg\}, \end{aligned}$$

with ρ^+, $(\rho u_x)^+$, $(\rho u_y)^+$, P_{xx}^+, P_{yy}^+, P_{xy}^+, N^+, J_x^+ and J_y^+ given explicitly in equation (A.24)–(A.31) of appendix A. In summary, $\mathbf{A}$ was defined implicitly above, in terms of its eigenvalues, λ_p, and its left row eigenvectors, $\mathbf{h}^{(p)}$, $p = 0, 1, ..., (Q-1)$, each of which determines one modal relaxation. The MRT scheme developed here and in appendix A has several novel features: (i) all dynamics corrections are made in evolution equation source term in equations (20)–(22) (or, equivalently, in the source terms of equation (26)), (ii) no explicit collision matrix, $\mathbf{A}$, is constructed and (iii) the post-collision distribution function is constructed directly from post-collision modes, $m^{(p)+}$, using equation (28).

Of course, species or colour is finally re-allocated according to f_i^+, using equation (9).

3.3. Velocity-dependent forces

For velocity dependent body force densities, the relationship between the first moment of lB's distribution function and the lattice fluid's macroscopic velocity requires attention. A body force and fluid velocity are generally related according to $\rho\mathbf{v} = \sum_i f_i \mathbf{c}_i + \frac{1}{2}\mathbf{F}$. If a component of $\mathbf{F}$ depends on $\mathbf{v}$, this relationship may be become implicit. Previous approaches to this general problem have involved approximate 'predictor-corrector' type methods [35] and algebraic solution [36]. Here, we begin by writing:

$$\rho\mathbf{v} = \sum_i f_i \mathbf{c}_i + \frac{1}{2}\left(\mathbf{F}(\mathbf{v}) + \mathbf{G}\right), \tag{30}$$

where $\mathbf{G}$ denotes any contribution to the total body force density which is velocity-independent, as in equation (34). Here, for $\mathbf{F}(\mathbf{v})$ given in equation (18), we find equation (30) may be solved. For the metric force density in equation (18), we obtain from equation (30) two decoupled partial differential equations (PDEs) for $\mathbf{v}$ as follows:

$$(\rho v_x, \rho v_z) = \sum_i f_i \mathbf{c}_i + \frac{1}{2}\eta\left(\frac{\partial}{\partial x}\left(\frac{v_x}{x}\right), \frac{1}{x}\frac{\partial v_z}{\partial x}\right) + \frac{1}{2}\mathbf{G}. \tag{31}$$

From equation (31), after a little algebra, we can write a pair of PDEs to be solved for v_x and v_z:

$$\begin{aligned}\frac{\partial v_x}{\partial x} - \left(\frac{1}{x} + \frac{2x}{\nu}\right) v_x &= -\frac{2x}{\nu}\frac{S_x}{S_0},\\ \frac{\partial v_z}{\partial x} - \frac{2x}{\nu} v_z &= -\frac{2x}{\nu}\frac{S_z}{S_0},\end{aligned} \tag{32}$$

where we have defined:

$$(S_x, S_z) = \sum_i f_i \mathbf{c}_i + \frac{1}{2}\mathbf{G}, \quad S_0 = \rho = \sum_i f_i, \tag{33}$$

so that $\mathbf{S}$ includes any contribution, $\mathbf{G}$, to the body force density which is velocity-independent. Relevant examples of the latter are the Lishchuk force for inter-facial tension effects and a buoyancy force:

$$\mathbf{G} = G_0 \hat{e}_z + \frac{1}{2}\sigma K \nabla \rho^N. \tag{34}$$

We seek v_x and v_z from PDEs (32) using integrating factors. We neglect spatial variation in $\mathbf{S}$ in order to obtain a tractable scheme. We will justify this approximation *a posteriori*. For the first of equation (32), an integrating factor is $\frac{1}{x}\exp\left(-\frac{x^2}{\nu}\right)$ and for the second, $\exp\left(-\frac{x^2}{\nu}\right)$. Accordingly, we can re-cast the first of equation (32) as $\frac{\partial}{\partial x}\left(v_x \frac{1}{x}\exp\left(-\frac{x^2}{\nu}\right)\right) = \frac{S_x}{S_0}\frac{1}{x}\frac{\partial}{\partial x}\exp\left(-\frac{x^2}{\nu}\right)$ whereupon integration by parts yields $\left(\frac{v_x}{x}\right)\exp\left(-\frac{x^2}{\nu}\right)\Big|_{x_0}^{\infty} = \frac{S_x}{S_0}\left[\frac{1}{x}\exp\left(-\frac{x^2}{\nu}\right)\Big|_{x_0}^{\infty} + \int_{x_0}^{\infty}\frac{1}{x^2}\exp\left(-\frac{x^2}{\nu}\right)\mathrm{d}x\right]$ and substituting limits, using transformation $u = \frac{x}{\sqrt{\nu}}$ and simplifying, we obtain for the pseudo-Cartesian lattice velocity x-component:

$$\begin{aligned} v_x &= \frac{S_x}{S_0} I(\nu, x),\\ I(\nu, x) &= \left[1 - \frac{1}{\sqrt{\nu}} x \exp\left(\frac{x^2}{\nu}\right)\int_{\frac{x}{\nu}}^{\infty}\frac{1}{u^2}\exp\left(-u^2\right)\mathrm{d}u\right].\end{aligned} \tag{35}$$

Numerical integration to determine $I(\nu, x)$ will be discussed shortly. Similarly, the second of equation (32) becomes $\frac{\partial}{\partial x}\left(v_z \exp\left(-\frac{x^2}{\nu}\right)\right) = -\frac{2x}{\nu}\exp\left(-\frac{x^2}{\nu}\right)\frac{S_z}{S_0}$, in which the right hand side is exact, hence $v_z \exp\left(-\frac{x^2}{\nu}\right) = \frac{S_z}{S_0}\exp\left(-\frac{x^2}{\nu}\right) + \phi(z)$ and selecting $\phi(y) = 0$, we have for the pseudo-Cartesian lattice velocity y-component:

$$v_z = \frac{S_z}{S_0}. \tag{36}$$

The factor $I(\nu)$ in equation (35) is evaluated, using Simpson's rule, for a range of x (transverse co-ordinate). Specimen data for $\nu = \frac{1}{6}$ are shown in figure 3. Note the integrand in $I(\nu)$, in equation (35), decays very rapidly indeed. This fact justifies our neglect of the spatial variation in the quantity $\frac{S_x}{S_0}$, above. For a given lattice position (x^*, z^*), the measured value of v_x is multiplied by $I(\nu, x^*)$. Naturally, scale-factors $I(\nu, x^*)$ may be pre-compiled for efficient computation. Note that, from equation (36), no adjustment to v_z is required in our pseudo Cartesian system.

The discussions above deal with the assignment of an appropriate velocity in a quasi 3D scheme. To simulate, one must of course be able to apply relevant boundary conditions. Appropriate kinetic scale simulation lattice closure rules and representation of the vertical boundaries $x = 0$ and $x \to \infty$ will be considered in section 4.

4. Simulations

We note that our pseudo-Cartesian methodology, reported above, reduces the computational expense of the complex flow validation simulations we describe below by at least two orders of magnitude.

To validate our pseudo Cartesian, MCLBE method (and with it the foundations of the chromo-dynamic variants' inter-facial kinematics and dynamics), we shall compare simulation data with analytical solutions. The latter exist, for curved interface configurations, only for steady flow. We first consider steady flow at $\mathrm{Re} = 0$ past a tethered, spherical drop, considered by Rybczynski [31] and Hadamard [32]. (See also [33] for a self-contained and contextualized treatment.) Second, we shall consider the perturbed solution of this flow, solved by Taylor and Acrivos [34], in which the drop deformation in flow is computed as a perturbation expansion in Weber, Wb, and Reynolds, Re, numbers. Figure 1(b) shows the simulation geometry of our test-bench solutions, which both require an unbounded external (blue) fluid.

Throughout this section, discrete lattice positions are indicated by use of an asterisk. The flows represented in schematic figure 1(B) were simulated as follows. Reported data correspond to a simulation lattice with $x^* = 0,1,..,199$ and $z^* = 0,1,..,299$, corresponding to $x = 0.5, 1.5, .., 199.5$ and $z = 0, 1, .., 299$. Horizontal periodic boundary conditions were applied between sites $z* = 0$ and $z^* = 299$, $\forall x^*$. The first lattice nodes in the domain, i.e. $x^* = 0$, were considered to lie at $x = 0.5$, to avoid a potential singularity in the source, A, at $x = 0$. Off the lattice boundary $x = 0$ is a symmetry condition, co-located with an inviscid, solid boundary condition, $v_n = 0$. Both these physical conditions were encapsulated in the applied lattice closure rule of mid-link specular reflection. A constant, positive body force density $-G_0\rho_R\hat{e}_z$ was applied. This body force produced acceleration, even for a neutrally buoyant drop, note.

For all data presented and discussed, the non-hydrodynamic, ghost, modes of our Dellar-type scheme were relaxed directly to equilibrium, by setting $\lambda_i = 1$ ($i \neq 3$) and the fluids' kinematic viscosity was $\nu = \frac{1}{3} =$ constant, (corresponding to the MRT relaxation parameter $\lambda_3 = \frac{2}{3}$). To facilitate comparison, our data will not depict the external flow. Of course, all velocity field data reported actually correspond to 3D, axially-symmetric flow, confined within (say) meridional planar section $\phi = 0$, taken from the equivalent 3D system.

4.1. Flow past a tethered spherical liquid drop

For the simulations performed on non-deforming drops, we shall utilize the fact that our test-bench analytical solution gives the flow field at all points. Accordingly, we present data for the entire flow field, which will facilitate our examination of inter-facial boundary conditions.

In the Re,Ca =0 regime, the anticipated micro-current activity will be relatively large, since micro-current amplitude is proportional to surface tension σ and the physical flow (value of U_0) must be small, to avoid deformation. Nevertheless, this artefact can be subtracted, to reveal the physical flow [35], even when it seemingly dominates. For clarity, we shall present data on internal flow within spherical drop and assume the kinematic viscosity of the system is uniform. Hence, the ratio of the shear viscosities is determined by the density contrast:

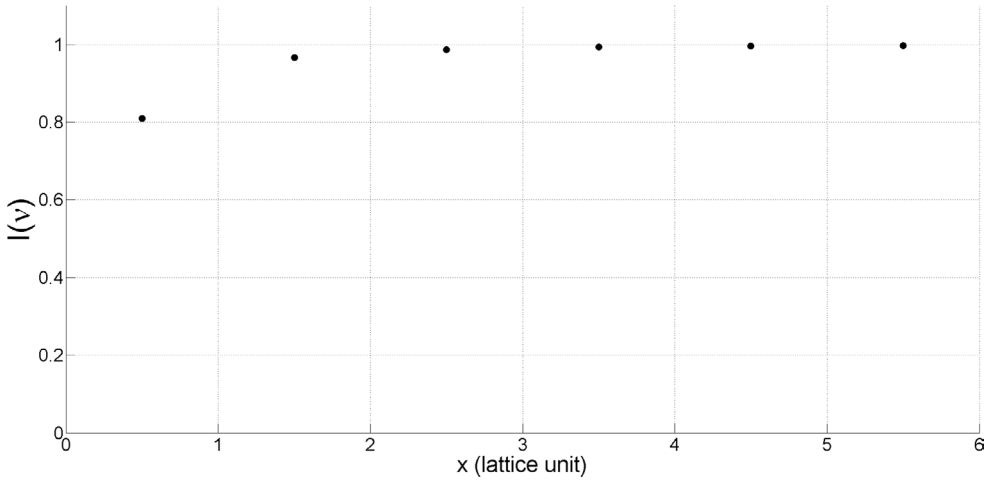

Figure 3. The result of a numerical integration, using Simpson's rule, for the multiplicative velocity scaling factor $I(\nu)$, defined in equation (35). For these data, $\nu = \frac{1}{6}$.

$$\frac{\eta_B}{\eta_R} = \frac{\nu\rho_{B0}}{\nu\rho_{R0}} = \frac{1}{\Lambda}.$$

The flow is most conveniently computed using a spherical polar co-ordinate system [33]. The analytical calculations [31, 32] represent a stringent test-bench and it makes explicit reference to key dynamic and kinematic boundary conditions, the representation of which in MCLBE simulation is our present concern. Note that the form of the theory quoted below does not contain explicit reference to inter-facial tension i.e. it refers only to kinematic and viscous, no-traction conditions at the interface and assumes surface tension forces are so strong as to enforce spherical shape. These constraints are raised when we come to consider a lightly deformed drop. Expressed in spherical co-ordinate system with the origin at drop centre, the internal velocity field is:

$$\begin{aligned} v_r^s &= \cos(\theta)\left(\frac{\Lambda}{1+\Lambda}\right)\frac{U_0}{2}\left(1-\frac{r_s^2}{R^2}\right), \\ v_\theta^s &= \sin(\theta)\left(\frac{\Lambda}{1+\Lambda}\right)\frac{U_0}{2}\left(1-\frac{2r_s^2}{R^2}\right), \\ v_\phi^s &= 0. \end{aligned} \tag{37}$$

Here, $U_0\hat{e}_z$ is the constant speed of the blue fluid at a large distance from the red drop and $r_s = \sqrt{r^2+z^2}$ is spherical polar distance from the origin. Note the stagnation point -the centre of a single internal vortex- is always located at $\theta = \frac{\pi}{2}$, $r_s = \frac{R}{\sqrt{2}}$ or, equivalently, $x = \frac{R}{\sqrt{2}}$, $z = 0$. This flow feature does not change position when Λ changes. The above solution is plotted as a vector field for $U = 1.0$, $R = 20$, in figure 4 (panel (A)).

In simulation, the steady-state of flow was identified by a constant velocity residual and the surface tension parameter, σ, used was always as small as possible for a front-back symmetric drop. A Galilean transformation to the rest frame of the drop was applied to the z velocity

component (only), once steady-state was reached. This was achieved by subtracting the average velocity of the red fluid, the latter being computed as a sum of annular mass increments:

$$v_z \to (v_z - \langle v_z \rangle) \tag{38}$$

$$\begin{aligned} \langle v_z \rangle &= \frac{\int\int_{r,z} 2\pi \rho_R(r,z) v_z(r,z) r \mathrm{d}r\mathrm{d}z}{\int\int_{r,z} \rho_R(r,z) r \mathrm{d}r\mathrm{d}z} \\ &\longrightarrow \frac{\sum_{x^*,z^*} 2\pi x^* \rho_R(x^*,z^*) v_z(x^*,z^*)}{\sum_{x^*,z^*} 2\pi x^* \rho_R(x^*,z^*)}. \end{aligned} \tag{39}$$

Hence, the simulated flow field was translated to the approximate rest frame of drop, translated z^* co-ordinates being rounded. Front-back symmetry and spherical drop shape were used to confirm that data correspond to $\mathrm{Re} \approx 0$. (Formally, the computed $\mathrm{Re} = \frac{<v_z>R}{\nu} < 3.0 \times 10^{-4}$.) The phase field of the steady state was then frozen, the applied body force removed and the corresponding micro-current flow allowed to evolve to its steady state. Finally, this flow was measured and subtracted. For all data reported in the next section, the value of phase field segregation parameter was $\beta = 0.67$ and the buoyancy parameter was $G_0 = 8.0 \times 10^{-9}$ lattice units. Data reported correspond to $R^* = 20$ lattice units and were checked for convergence to the narrow interface limit and for general finite size effects as follows. Our check for finite size effects was performed by taking a system with size parameters $R^* = 20$ lattice units, $x^* \in [0, 199]$, $z^* \in [0, 299]$ and repeatedly doubling x^*, z^* whilst keeping R^* fixed; our check for the narrow interface (continuum) limit was performed by repeatedly doubling all of x^*, z^*, R^*.

4.2. Flow past a tethered deforming drop

For these simulations, we shall present data for the drop shape deformation alone, for which analytic expressions exist. This validation is therefore more challenging to interpret that that reported in section 4.1 above.

Taylor and Acrivos use a singular perturbation solution of the antisymmetric equations of motion to predict the shape (and drag) of a slightly deforming drop [34]. We shall be concerned with Taylor and Acrivos' equation (30) and will use their notation. With our restriction of equal kinematic viscosities, the deformed drop radius at spherical polar zenithal location, θ, may be written:

$$\frac{R(\theta)}{R} = 1 - a_2 P_2(\cos(\theta)) - a_3 P_3(\cos(\theta)) + ..., \tag{40}$$

with expansion co-efficients [34]:

$$a_2 = \lambda We, \quad a_3 = \frac{3\lambda(11\Lambda + 10)}{70(\Lambda + 1)} \frac{We^2}{\mathrm{Re}}, \tag{41}$$

where $P_2(x)$ etc is the second order Legendre polynomial [29] and:

$$\lambda = \frac{1}{4(\Lambda+1)^3} \left[\frac{81}{80}\Lambda^3 + \frac{83}{30}\Lambda^2 + \frac{103}{40}\Lambda + \frac{5}{6} \right]. \tag{42}$$

No confusion should arise from our use of symbol λ above, as the MRT collision eigenvalues, λ_p, $p = 1, ..., 3$. In simulation, we compute dimensionless Reynolds and Weber numbers as follows:

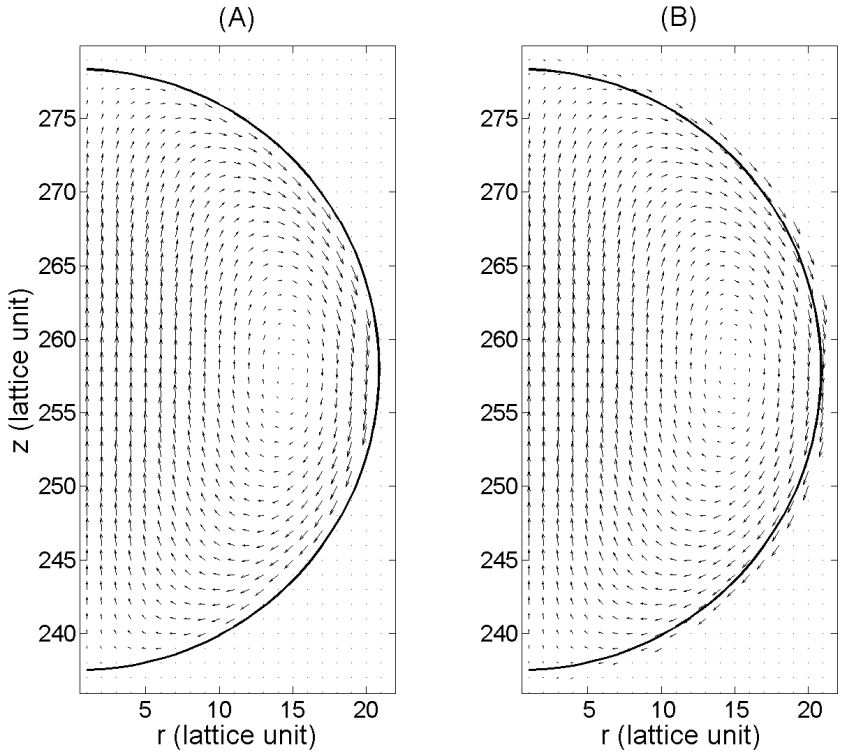

Figure 4. Comparison between analytical internal solution of flow past an effectively tethered red drop and simulation results. Panel (A) shows the analytical solution stated in equation (37). Note, the analytical solution has been shifted in z to facilitate comparison with the micro-current adjusted simulation data in the second panel, (B). Both velocity fields are separately normalised by our plotting package (Matlab ver. 2014b.). The solid black contour shows the nominal position of the interface, $\rho^N = 0$ contour. For these data: $R = 20$, $x \in [0.5, 199.5]$, $z \in [0, 299]$, $\beta = 0.67$, buoyancy parameter $G_0 = 8.0 \times 10^{-9}$ and $\nu = \frac{1}{6}$.

$$\mathrm{Wb} = \frac{\rho_B < v_z >^2}{\Delta p}, \quad \mathrm{Re} = \frac{R < v_z >}{\nu}, \tag{43}$$

where Δp is the measured pressure step across the drop interface, from equation (6). Simulations were performed as described in section 4.1, above. Data for the deformed radius were extracted and fitted to equation (40) as set-out below, by first computing the centre of gravity as:

$$\begin{aligned} \langle z \rangle &= \frac{\int\int_{rz} 2\pi z \rho_R(r,z) r \mathrm{d}r\mathrm{d}z}{\int\int_{rz} 2\pi \rho_R(r,z) r \mathrm{d}r\mathrm{d}z} \\ &\longrightarrow \frac{\sum_{x^*,z^*} 2\pi x^* \rho_R(x^*,z^*) z^*}{\sum_{x^*,z^*} 2\pi x^* \rho_R(x^*,z^*)} \end{aligned} \tag{44}$$

and from it the radial distance and zenithal angle of inter-facial locations $(x^*, z^*) : \rho^N(x^*, z^*) \in [-0.2, 0.2]$ were computed as follows:

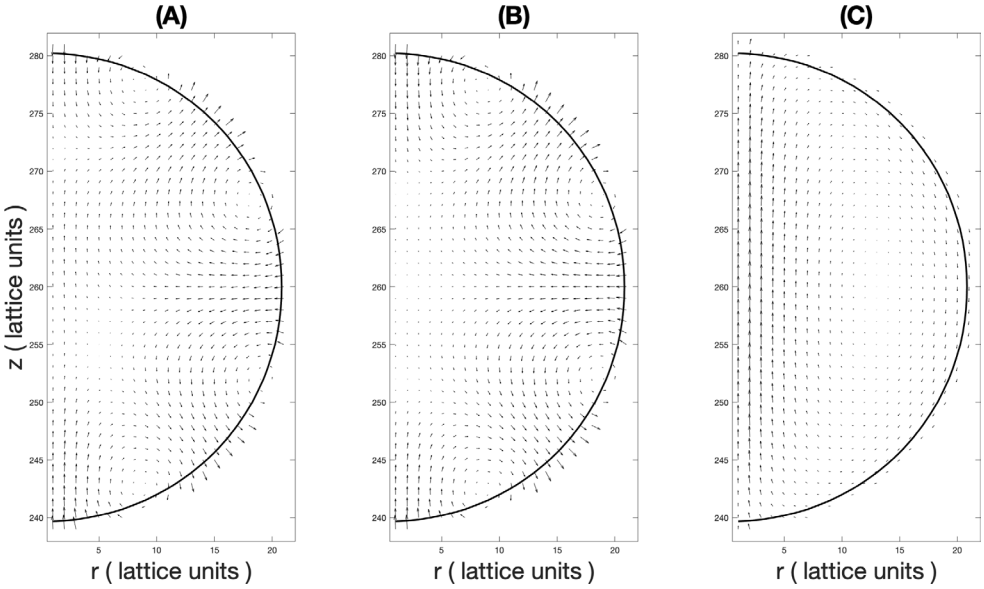

Figure 5. Flow past an effectively tethered red drop, here centred close to the location $z^* = 260$ lattice units. The solid line is the contour $\rho^N = 0$. The flow of the external, blue fluid has not been plotted. Panel (A) shows the scaled velocity field after application of the transformation in equations (38) and (39). The effect of the inter-facial micro-current is very clear. Panel (B) shows the steady-state micro-current computed for the phase field configuration in (A) without any external flow. Panel (C) shows the result of subtracting the flow in (B) from that in (A). The correspondence with theory and, in particular, the compliance of the flow with the kinematic condition are striking in the data in panel (C). In particular, the physical flow in panel (C) lies tangent to the interface. Simulation data as figure 4.

$$R(\theta^*) = \left((x^* + 0.5)^2 + (z^* - < z >)^2\right)^{1/2},$$
$$\theta^* = \cos^{-1}\left(\frac{z^* - < z >}{R^*}\right). \tag{45}$$

A conjugate gradients grid search optimised a fit to equation (40), using as adjustable parameters the undeformed drop radius, R, and amplitudes a_2, a_3 should, apparently, produce results related to Wb and Re after equation (41). For deformed drop data presented in section 5, the value of the phase field segregation parameter was reduced to $\beta = 0.3$, with a commensurate doubling of undeformed drop radius (to $R^* = 40$) and lattice dimensions. This was necessary to stabilize simulations, whilst maintaining the width of the inter-facial region (which varies as $1/\beta$), relative to R, constant compared with data in section 4.1. The surface tension parameter $\sigma = 6.0 \times 10^{-4}$ lattice units, $\mathrm{Wb} \leqslant 2.0 \times 10^{-2}$ and $\mathrm{Re} < 0.1$.

5. Results and discussion

All data presented and discussed in this section correspond to maximum density contrasts $\Lambda < 10$. We return to this matter in our conclusions. The main interest of this article is not

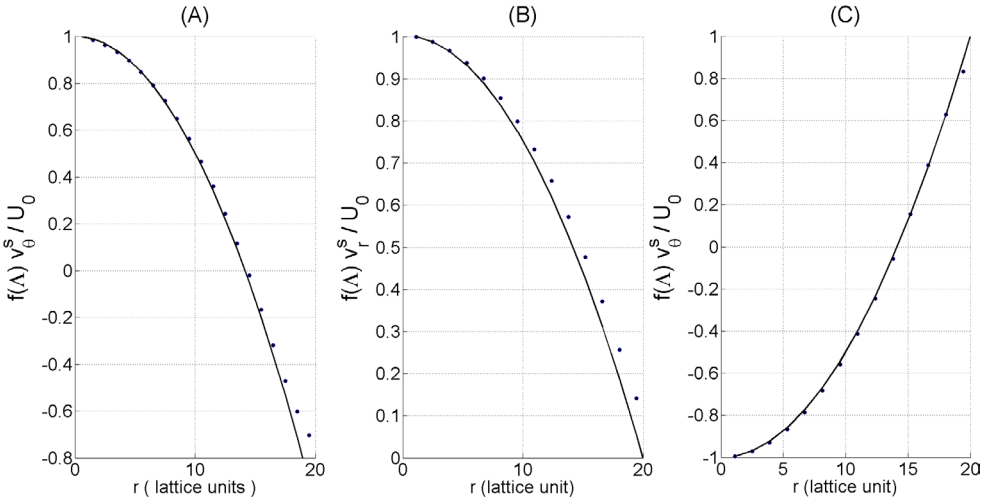

Figure 6. Normalised velocity field components from figure 5 (C) along two transects, from am un-deformed, spherical drop centre, with $\Lambda = 5$. The continuous line corresponds to theory (equation (37)), points to simulation data. Panel (A) compares the spherical polar radial velocity with its measured value along the equator (Note that there is no tangential component of motion along the drop equator). Panel (B) compares the spherical polar radial velocity with its measured value along a line sub-tending an angle of $\frac{\pi}{4}$ at the positive z axis. Panel (C) : as panel (B) but for the tangential component of velocity. Simulation data as figure 4.

the stability of the chromo-dynamic density difference method, rather it is the fundamental accuracy of its hydrodynamics. In this respect, results are encouraging.

Consider our first test-bench solution of flow past a spherical, red tethered drop, as discussed in section 4.

Figure 4 below shows, side by side, the full velocity field of the shifted analytical solution, computed from spherical polar co-ordinate velocity components in equation (37) (panel (A)) and the corresponding velocity field obtained from simulation (panel (B)). The latter were adjusted for the micro-current as discussed shortly. For these data, $\Lambda = 1$. The correspondence between these two solutions over the whole internal domain is excellent.

Panel (A) of figure 5 shows steady-state simulation data for the scaled internal velocity field, after applying the Galilean transformation in equation (39). In these data, the effect of the inter-facial micro-current is very clear and flow is certainly not parallel to the interface (the solid black contour corresponds to the interface center, $\rho^N = 0$). A localized micro-current circulation may be subtracted from the overall flow in (A), to reveal the physical flow in the linear, Stokes' regime [35]. The flow in panel (B) of figure 5, which is *not* normalised to the same quantity as that in panel (A), corresponds to the micro-current of the 'frozen' colour field, ρ^N. This is subtracted, vectorally, to expose the physical flow field in panel (C). The correspondence with theory and, in particular, the compliance of the flow with the kinematic condition of mutual impenetrability are striking in these data. Whilst a MCLBE interface is not sharp, flow is directed tangentially to contours of $\rho^N =$ constant everywhere within a shell of finite thickness and we can say that the physical flow lies tangent to the curved interface at all relevant points in the simulated domain. The significance of this result should be stressed. Apparently, in this challenging Re, Ca =0 regime, where received wisdom would argue that the influence of the inter-facial micro-current is proportionally large in comparison with the

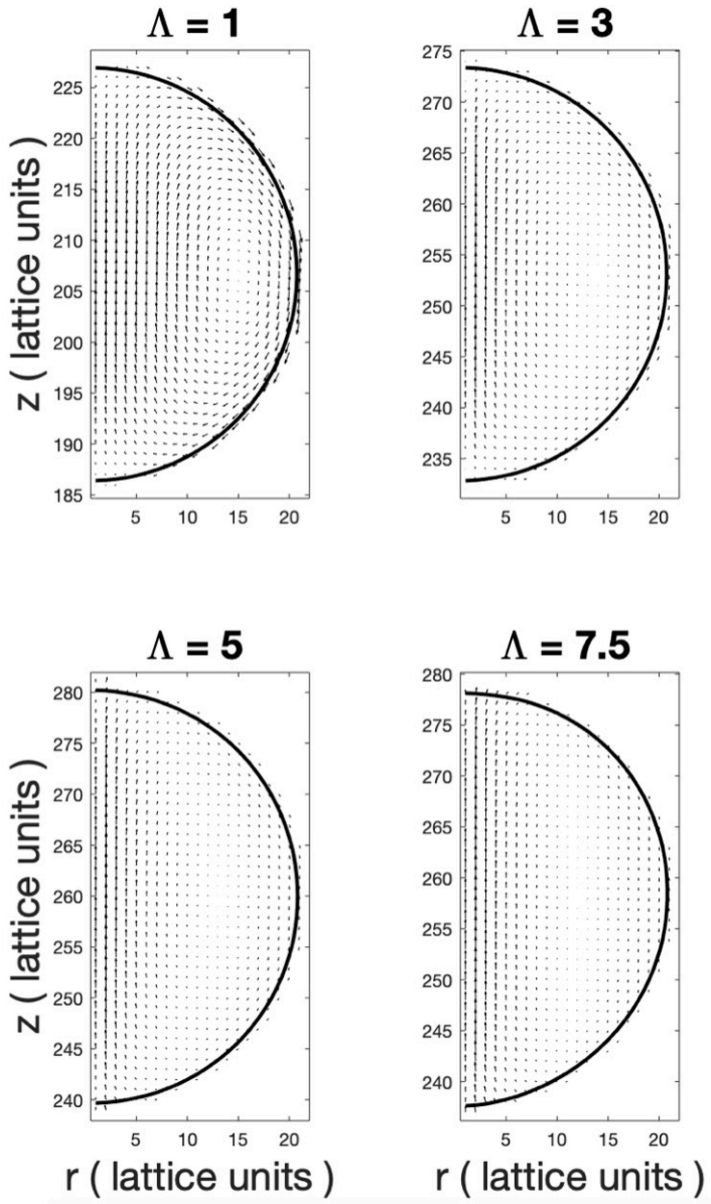

Figure 7. Corrected flow field (i.e. with the inter-facial micro-current removed), for flow past an effectively tethered red drop computed, for a range of density contrasts, Λ, in Stokes' regime (All flows have Re$< 2 \times 10^{-4}$). External flow of the blue fluid is not plotted. The solid line is the contour $\rho^N = 0$. The plotting package used (MATLAB) has normalised the flow depicted in each panel individually. Nevertheless, it is clear that, in all cases, the location of the primary vortex agrees with the prediction in equation (37). (That is, the vortex is predicted to lie at $x = r = \frac{R}{\sqrt{2}}$, $\forall \Lambda$). Moreover, the extent of compliance with the kinematic condition of mutual impenetrability across the range of Λ is also clear in these data.

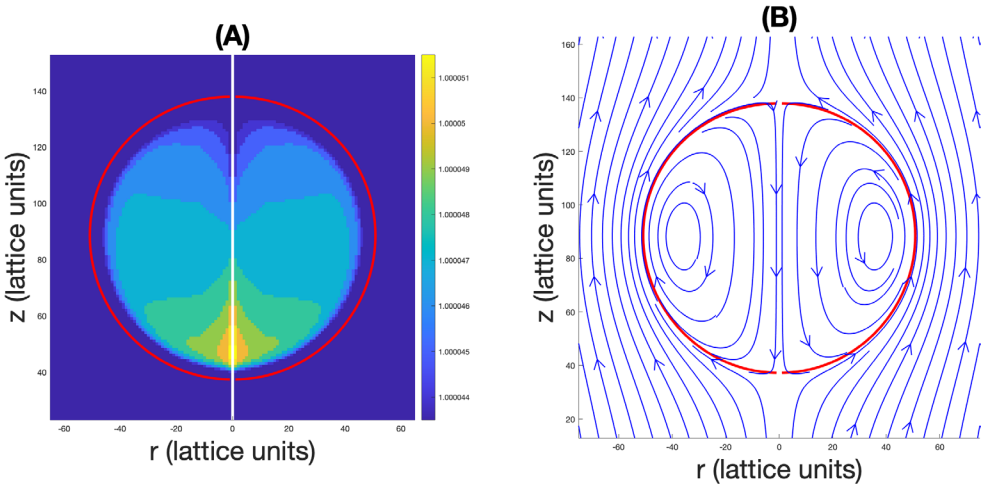

Figure 8. Signals in a meridional section through a lightly deformed drop sedimenting vertically downwards, viewed from the rest frame of the drop, at steady state. Panel (A) shows the pressure field (in lattice units). Panel (B) shows Stokes' stream-function. The red contour shows the $\rho^N = 0$ contour. For these data, $\beta = 0.3$, $\Lambda = 5$, $R = 40$, $x^* = 0.5,1.5,...,300$, $y^* = 0,1,...,400$, $\nu = \frac{1}{6} = \text{constant}$.

true, hydrodynamic signal, our data, together with the supporting analysis contained in [24], demonstrate that, at steady state, its influence may be removed altogether, simply by computing, then subtracting the flow induced by the frozen phase field, ρ^N. Figure 6 assesses the quantitative variation of the velocity field components from figure 5(C), measured along two transects from the lattice co-ordinate closest to the drop centre. To facilitate comparison with the theory of equation (37) we have defined:

$$f(\Lambda) = \left(\frac{1+\Lambda}{\Lambda}\right). \tag{46}$$

Panel (A) compares the spherical polar radial velocity, v_r^s, with its measured value along the equator ($\theta = 0$), where there is no tangential component of motion, note. Panel (B) compares spherical polar v_r^s with its measured value along the line subtending an angle of $\frac{\pi}{4}$ at the positive z axis, intersecting the latter close to the centre of the drop (i.e. $\theta \approx \frac{\pi}{4}$). Panel (C) : as panel (B) but for spherical polar v_θ^s. In these data, correspondence between theory and simulation is weakest for $r \to R$ as expected, owing to the diffuse nature of the MCLBE interface. In simulation, the interface corresponds to a shell of finite thickness, not a surface. Again, we observe that despite its diffuse nature, both the magnitude and direction of flow conform with a sensible interpretation of the relevant continuum no-traction and kinematic conditions. In figure 7, we show the simulated internal flow field (with the inter-facial micro-current removed, as discussed above), for flow past an effectively tethered red drop computed, for a range of density contrasts, Λ, all in Stokes' regime. (All flows have Re$< 2 \times 10^{-4}$.) Note that the buoyancy parameter varies between the data on panels (A)..(D). Insofar as one can judge from these data, the location of the primary vortex does not change, which agrees with the prediction implicit in equation (37). Moreover, the extent of compliance with the kinematic condition of mutual impenetrability, across the range of Λ is again very clear in these data. We defer all further discussion until section 6.

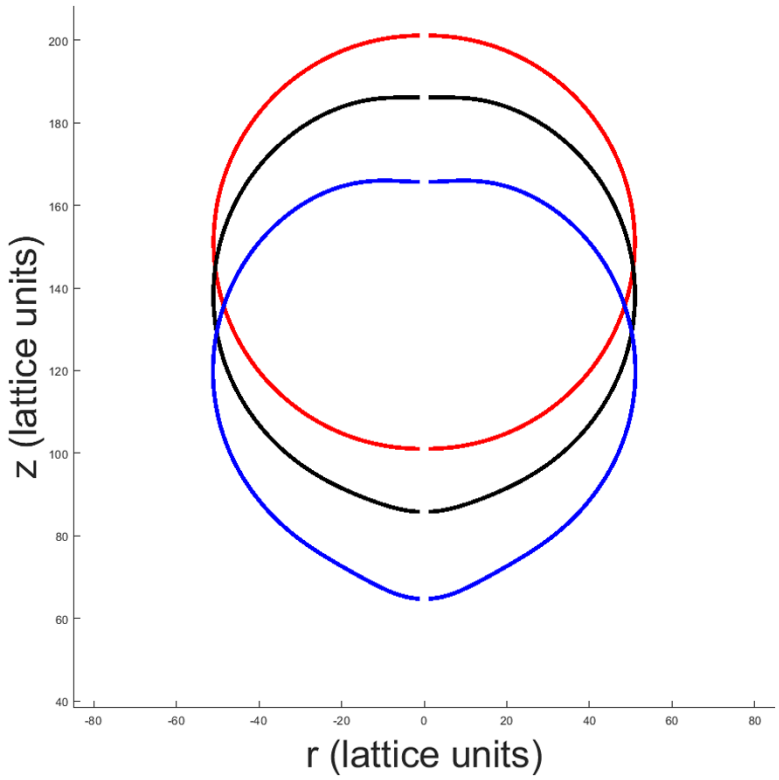

Figure 9. Time development of deformation. Sequential interface configurations for a drop sedimenting vertically downwards (displacement not to scale). The red red line corresponds to the initial $\rho^N = 0$, the black contour is a later time and the blue contour corresponds to steady state. For these data, $\Lambda = 5$ with all other parameters as figure 10.

We proceed to consider our second test-bench solution of flow past a slightly deformed drop. It will be noted that the range of Λ achieved with the chosen level of resolution, for this more complex interface shape is reduced relative to that in e.g. figure 4. We return to this issue in section 6.

Figure 8 shows data obtained for a drop sedimenting vertically downwards, with deformation, viewed from the rest frame of the drop, at steady state. For these data, $\Lambda = 5$. Panel (A) shows the pressure field (in lattice units), panel (B) shows Stokes' stream-function for the flow, whilst the red contour corresponds to the $\rho^N = 0$ contour, which is the nominal interface. In figure 9 we see the time development of deformation in a set of interface configurations for a drop sedimenting vertically downwards. Here, the red line corresponds to the initial $\rho^N = 0$ contour, the black contour is a later time and the blue contour corresponds to steady state.

In figure 10 we see points on the lightly deformed drop interface for $\mathrm{Wb} \approx 2.0 \times 10^{-2}$, $\mathrm{Re} \approx 0.01$, for three lightly deformed drops with $\Lambda = \frac{1}{2}, 1, 2$ (panels (A), (B), (C) respectively). The solid line corresponds to a conjugate gradients grid search optimised fit to the prediction of equations (40)–(42). The measured fit coefficients corresponding to these data are recorded in table 2, below.

The fit to the interface is in reasonable agreement with the predictions of analytical perturbation theory.

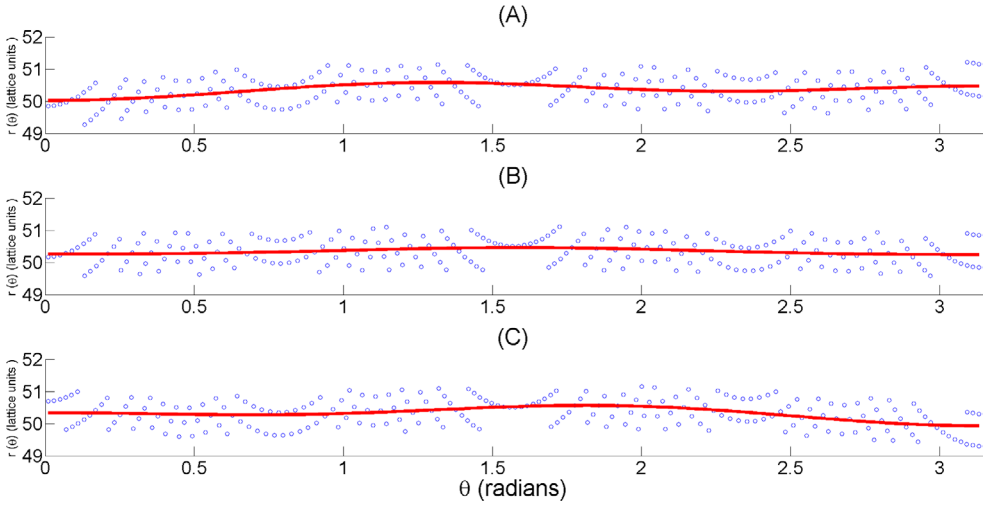

Figure 10. Fits to the deformed interface of a moving drop with Wb ≈ 0.02. The continuous red line is an optimum fit to the perturbation calculation summarized in equations (40)–(42). Panel (A) $\Lambda = 0.5$, (B) $\Lambda = 1.0$, (C) $\Lambda = 2$. For these data, phase field segregation parameter $\beta = 0.3$, $R^* = 40$, $x^* = 0,1,..,600$, $y^* = 0,1,..,400$ surface tension parameter $\sigma = 6.0 \times 10^{-4}$ lattice units, Wb $\leqslant 2.0 \times 10^{-2}$ and Re <0.1.

Table 2. Measured drop deformation. The value of parameter a_2 measured by fitting interface data (see figure 10) is compared with that computed from equation (41), using the measured value of Wb (column 1) and the value of λ in equation (42).

Wb	Λ	a_2 simulation	a_2 theory
0.019 123	0.50	−0.208 83	−0.209 88
0.019 043	1.00	−0.151 21	−0.215 46
0.022 791	2.00	−0.268 77	−0.267 41

6. Conclusion

Here, we have developed a 2D pseudo Cartesian, chromo-dynamic MCLBE scheme for efficient simulation of multi-component systems with 3D axial symmetry, continuously distributed sources (and/or sinks) of momentum and a density contrast between the simulated fluids. This methodology makes the complex inter-facial validations we report computationally accessible. Without our 2D pseudo Cartesian model, our simulations would have been at least two orders of magnitude more expensive. Our analysis motivates a novel and versatile treatment for velocity-dependent forces in lattice Boltzmann methodology (here, the metric force terms of the cylindrical Navier–Stokes equations), which should facilitate wider application of the method, where such forces are present e.g. magneto-hydrodynamics, porous flow and geophysical flow. All the data we present with our novel scheme correspond to maximum density contrasts of $\Lambda \approx 10$. The investigations of Burgin *et al* [24], using a similar chromo-dynamic MRT model in 2D only achieve larger Λ in the case of no applied flow. Moreover, the complex simulations with chromo-dynamic MCLBE method [20] have $\Lambda = 2$. Apparently, the density contrasts achievable with a given level of resolution appear to be less than those achieved with the MCLBE method of e.g. Innamuro *et al* [37]. Nevertheless flows of immiscible fluids at

this level of density contrast are important in many chemical engineering and environmental applications, where verified inter-facial hydrodynamics may be more important than the the scale of Λ.

The methodological developments we relate here facilitate our principal aim: validation of interfacial hydrodynamic properties of chromo-dynamic MCLBE, with complex interface shapes, by computation of solved problems, namely flow past a spherical liquid drop for Re,Ca $\rightarrow 0$ and, also, a lightly deformed drop. A glance at figure 5 illustrates the question. In panel (A), the dominant micro-current produces a strong transverse flow, which clearly violates the kinematic of condition of mutual impenetrability. However, in the case of a spherical drop, simulation data, once corrected for the inter-facial micro-current (see below), actually show excellent agreement with well-accepted analytical theory, over a range of density contrasts and strongly imply the operation of the kinematic condition of mutual impenetrability (e.g. figure 4) and the no-traction condition (e.g. figure 6). Broadly, agreement between data from chromo-dynamic MCLBE variants (including those with sources, herein) and the kinematic condition of mutual impenetrability is very good for flat interfaces [24] and, we now confirm, also for curved interfaces in 3D flows. This result clearly adds considerable support to a number of recent chromo-dynamic MCLBE, MRT schemes [17, 19, 20], as well as future applications with the method. Further, for lightly deformed drops, simulation data are in reasonable agreement with analytical theory,

The excellent agreement obtained in the challenging Re $=0$, Ca $\rightarrow 0$ regime, in which the inter-facial micro-current is a relatively large contribution to the total flow, shows the precaution of phase field freezing, outlined in section 5, to be a very effective means of resolving the physical flow alone. Generally, the success of this procedure supports the view that the inter-facial micro-current is a super-posed, hydrodynamic response in the linear regime (which implies that interfacial micro-currents in other MCLBE variants can be removed in a similar fashion). It also provides a way forward for the use of MCLBE throughout suspension rheology, especially in the limit of a high volume fraction of the suspended phase, where micro-current activity infects -indeed, dominates- hydrodynamic signals over most of the domain.

Appendix A. Multi-relaxation-time scheme for large density contrast immiscible fluids with density sources/sinks

We present a detailed derivation of the Navier–Stokes equations from the multiple-relaxation-time (MRT) lattice Boltzmann equation adapted for multi-component applications with a large density difference between completely immiscible components, where a body force is present. The latter is necessary to carry the Lishchuk interface force. Density gradients associated with a chromo-dynamic or phase field must not affect the macroscopic dynamics, of course. Equally the dynamics of the developed scheme should not affect the physics of the segregation rule. The challenge is to compensate for their presence accurately, whilst retaining algorithmic stability and simplicity. The key advance outlined in this appendix is the consideration of fluid cources and sinks.

In the interest of a compact literature, we retain here the overall structure of the analyses of Guo *et al* [14], Dellar [25] and Hou *et al* [26]. For this reason we work in this appendix in two dimensions, using space variables x and y and we denote flow velocity $\mathbf{u}$. We choose to extend the scheme of Dellar because it is efficient (due to a careful choice of non-hydrodynamic modes N, J_x and J_y [25] with zero equilibria), robust, straightforward to implement and, not least, logical. Note, within this and following appendices, $\sum_i = \sum_i^{(Q-1)}$.

At the kinetic scale, the 'forced' MRT LBE for a system subject to an 'external' force term can be expressed in the following form:

$$f_i\left(\mathbf{x}+\mathbf{c}_i\delta_t, t+\delta_t\right) = f_i(\mathbf{x},t) + \sum_j A_{ij}\left[f_j^{(0)}(\mathbf{x},t) - f_j(\mathbf{x},t)\right] + \delta_t F_i, \tag{A.1}$$

where the density-difference supporting equilibrium distributes mass away from the rest $(j=0)$ link via term ϕ_j, is in the form of:

$$f_j^{(0)} = \rho\phi_j + \rho t_j\left(3u_\alpha c_{j\alpha} + \frac{9}{2}u_\alpha u_\beta c_{j\alpha}c_{j\beta} - \frac{3}{2}u_\gamma u_\gamma\right),$$

and where the kinetic equation source term, F_i, is assumed to have the following properties:

$$\sum_i F_i = A,\ \sum_i \mathbf{c_i}F_i = n\mathbf{F},$$
$$\sum_i c_{i\alpha}c_{i\beta}F_i = c_s^2 A\delta_{\alpha\beta} + \frac{1}{2}\left[C_{\alpha\beta} + C_{\beta\alpha}\right],$$

where n is a scalar to be determined and tensor $\mathbf{C}$ is also to be determined.

In this appendix, we first set-out the basics, then proceed to the Chapman–Enskog analysis to obtain the thermodynamic limit of the kinetic scheme defined in equation (A.1) (i.e. find appropriate expressions for tensor $\mathbf{C}$, which represents the crux of the problem of recovering correct hydrodynamics with the MRT scheme), then we transform to a modal description, and finally, we invert that transformation to obtain an explicit expression for the post-collision distribution function. To maintain parity with the analysis of Guo *et al* [14] at the outset, we now 'relax' the form of the definition of lattice velocity given in equation (3) as follows:

$$\rho\mathbf{u} = \sum_i f_i(\mathbf{r},t)\mathbf{c}_i + m\mathbf{F},$$

with m being a constant to be determined.

Dellar's [25] eigenvalues and left row eigenvectors for the collision matrix A_{ij} can be tabulated as in table 1, where we define

$$P_{\alpha\beta} \equiv \Pi_{\alpha\beta}^{(0)} + \Pi_{\alpha\beta}^{(1)}, \tag{A.2}$$

for $\alpha,\ \beta = x, y$, and the $\Pi_{\alpha\beta}^{(p)}$, $p = 0, 1$ have the usual meaning, which is also set-out later in this appendix.

As set out in table 1, matrix A_{ij} has the following properties which, it will be seen, are necessary if one is to recover correct hydrodynamics:

$$\sum_i 1_i A_{ij} = 0, \tag{A.3}$$

$$\sum_i c_{i\alpha}A_{ij} = 0, \tag{A.4}$$

$$\sum_i c_{i\alpha}c_{i\beta}A_{ij} = \lambda_3 c_{j\alpha}c_{j\beta}. \tag{A.5}$$

Here α and β represent either x or y direction in the lattice grid. We also assume that the lattice basis $\mathbf{c_i}$ and the corresponding weights t_i have the following symmetry properties:

$$\begin{aligned}
\sum_i t_i &= 1, \\
\sum_i t_i (c_{i\alpha})^{2p+1} &= 0, \quad p \geqslant 0 \\
\sum_i t_i c_{i\alpha} c_{i\beta} &= \frac{1}{3}\delta_{\alpha\beta}, \\
\sum_i t_i c_{i\alpha} c_{i\beta} c_{i\gamma} c_{i\theta} &= \frac{1}{9}\left(\delta_{\alpha\beta}\delta_{\gamma\theta} + \delta_{\alpha\gamma}\delta_{\beta\theta} + \delta_{\alpha\theta}\delta_{\beta\gamma}\right),
\end{aligned} \tag{A.6}$$

where $\delta_{\alpha\beta}$ is the Kronecker delta such that $\delta_{\alpha\beta} = 1$ for $\alpha = \beta$, and 0 otherwise. Weightings t_i are effectively the same as found in Hou *et al* [26]; that is $t_0 = \frac{4}{9}$, $t_{\text{odd}} = \frac{1}{36}$ and $t_{\text{even}} = \frac{1}{9}$. (See figure 2 for the definition of our link vectors and indexing.) Note that the six left row eigenvectors $\mathbf{h}^{(0)}, .., \mathbf{h}^{(5)}$ which appear in equations (A.3)–(A.5), as defined in table 1, are linearly independent but not orthogonal. We will return to this matter later. We follow Benzi *et al* [27, 28] and Dellar [25] in selecting the other three 'ghost' eigenvectors (see table 1), in respect of which it is important to note the choice:

$$g_0 = 1, \quad g_{\text{odd}} = 4, \quad g_{\text{even}} = -2,$$

where the designation 'odd' indicates the value applies to long lattice links, with values of subscript i.

Our equilibrium distribution function $f_i^{(0)}$ may now be shown to have the following properties, which, again, are necessary if one is to recover correct hydrodynamics:

$$\sum_{i=0}^{Q-1} f_i^{(0)}(1, c_{i\alpha}, c_{i\alpha}c_{i\beta}) = \left(\rho, \rho u_\alpha, (2\phi_1 + 4\phi_2)\rho\delta_{\alpha\beta} + \rho u_\alpha u_\beta\right). \tag{A.7}$$

Functions ϕ_1 and ϕ_2 depend upon the chromo-dynamic field (see equation (4)) and hence the spatial-temporal variation of the isotropic term of the second moment is modified as follows: $\sum_i f_i^{(0)} c_{i\alpha} c_{i\beta} = \left[\frac{3}{5}\left((1-\alpha_R)\rho_R + (1-\alpha_B)\rho_B\right)\delta_{\alpha\beta} + \rho u_\alpha u_\beta\right]$. Here, the variation of the speed of sound between red and blue components is apparent, with $c_{sR}^2 = \frac{3}{5}(1-\alpha_R)$ and $c_{sB}^2 = \frac{3}{5}(1-\alpha_B)$.

We now proceed with a Chapman–Enskog expansion of the kinetic equation and distribution function. The latter is used to expand f_i around the equilibrium and to reflect the changes occurring at different time scales, as follows:

$$\begin{aligned}
f_i &= f_i^{(0)} + \epsilon f_i^{(1)} + \epsilon^2 f_i^{(2)} + \cdots, \\
\frac{\partial}{\partial t} &= \frac{\partial}{\partial t_0} + \epsilon\frac{\partial}{\partial t_1} + \epsilon^2\frac{\partial}{\partial t_2} + \cdots.
\end{aligned}$$

The expansion parameter ϵ can be interpreted as the Knudsen number, which is proportional to the ratio of the lattice spacing to the characteristic flow length. Clearly, the assumptions expressed in equation (A.7) imply $\sum_i f_i^{(p)} = 0$ and $\sum_i f_i^{(p+1)}\mathbf{c_i} = 0$, $p \geqslant 1$ but it is important to note that:

$$\rho\mathbf{v} = \sum_i f_i \mathbf{c}_i + m\mathbf{F}\delta_t \quad \Leftrightarrow \quad \sum_i f_i^{(1)}\mathbf{c}_i = -m\mathbf{F}\delta_t.$$

Let us consider the most rapid behaviour in the model. Equation (9b) of [14] (Guo *et al*) can be obtained straightforwardly as the following:

$$O(\epsilon): \quad (c_{i\alpha}\partial_\alpha + \partial_{t_0}) f_i^{(0)} = -\frac{1}{\delta_t}\sum_j A_{ij} f_j^{(1)} + F_i. \tag{A.8}$$

Taking summation $\sum_i$ on both sides of equation (A.8) leads to:

$$\partial_\alpha \sum_i f_i^{(0)} c_{i\alpha} + \partial_{t_0}\sum_i f_i^{(0)} = -\frac{1}{\delta_t}\sum_{ij} A_{ij} f_j^{(1)} + \sum_i F_i$$
$$= A.$$

Using property (A.3), we therefore obtain:

$$\partial_\alpha \rho u_\alpha + \partial_{t_0}\rho = A.$$

which gives the continuity equation and is the MRT equivalence of equation (10a) in [14]. Before proceeding further, we present the counterpart result, deriving from the kinematics of our model. It is reasonable to interpret equation (11), which is order δ_t accurate, as corresponding to the statement $\frac{D\rho_R}{Dt} = \frac{D\rho_B}{Dt} = 0$, from which it is straightforward to deduce [24]:

$$\frac{D\rho^N}{Dt_0} = 0. \tag{A.9}$$

That is, on the shortest timescales, the chromo-dynamic field is a material invariant. We will indicate where we appeal to this fact, to eliminate certain t_0 derivatives, as we proceed. Multiplying every term of equation (A.8) by c_{ix} and taking summation $\sum_i$ on both sides, we have:

$$\sum_i (c_{i\alpha}\partial_\alpha + \partial_{t_0}) f_i^{(0)} c_{ix} = -\frac{1}{\delta_t}\sum_{ij} c_{ix} A_{ij} f_j^{(1)} + \sum_i F_i c_{ix}, \tag{A.10}$$

where $\sum_i F_i c_{ix} = nF_x$, n is a constant to be determined, and we will use property (A.4). Similar as in [26] (Hou *et al*), the momentum flux tensor is defined as:

$$\Pi_{\alpha\beta}^{(p)} = \sum_i f_i^{(p)} c_{i\alpha} c_{i\beta}, \quad p = 0, 1. \tag{A.11}$$

Equation (A.10) can be simplified to produce the Euler equation:

$$\partial_\alpha \Pi_{\alpha x}^{(0)} + \partial_{t_0}\rho u_x = nF_x, \tag{A.12}$$

where the zeroth-order momentum flux tensor $\Pi_{\alpha x}^{(0)} = (2\phi_1 + 4\phi_2)\rho\delta_{\alpha x} + \rho u_\alpha u_x$ and $\delta_{\alpha x}$ is the Kronecker delta. Equation (A.12) is the MRT equivalence of (10b) in [14] Guo *et al*. We note that the equivalent result in Guo *et al* [14] couples n, m and τ (the collision parameter) in the case of the single-relaxation time (SRT) variant. Following Guo *et al* [14] we recover the appropriate form of the Euler equation by setting:

$$n = 1,$$

with no constraint on m at $O(\epsilon)$.

Proceeding to $O(\epsilon)^2$ in the Chapman–Enskog expansion, equation (9c) of [14] can be rewritten as the following:

$$O(\epsilon^2): \partial_{t_1} f_i^{(0)} + (c_{i\alpha}\partial_\alpha + \partial_{t_0}) f_i^{(1)} - \frac{1}{2}(c_{i\alpha}\partial_\alpha + \partial_{t_0}) \sum_j A_{ij} f_j^{(1)}$$
$$= -\frac{1}{2}(c_{i\alpha}\partial_\alpha + \partial_{t_0})\delta_t F_i. \tag{A.13}$$

Taking summation $\sum_i$ on both sides of equation (A.13) and simplifying the result gives:

$$\partial_{t_1}\rho = \left(m - \frac{n}{2}\right)\delta_t \partial_\alpha F_\alpha - \frac{1}{2}\partial_{t_0} A,$$

which is equivalent to (13a) of [14]. We recover appropriate dynamics by requiring:

$$m - \frac{n}{2} = 0 \;\Leftrightarrow\; m = \frac{1}{2}.$$

A similar treatment can be performed on equation (A.13) by multiplying every term by c_{iy} and taking summation $\sum_i$ on both sides:

$$\partial_{t_1}\sum_i f_i^{(0)} c_{iy} + \partial_\alpha \sum_i f_i^{(1)} c_{i\alpha} c_{iy} + \partial_{t_0}\sum_i f_i^{(1)} c_{iy}$$
$$-\frac{1}{2}\partial_\alpha \sum_{ij} c_{i\alpha} c_{iy} A_{ij} f_j^{(1)} - \frac{1}{2}\partial_{t_0}\sum_{ij} c_{iy} A_{ij} f_j^{(1)}$$
$$= -\frac{1}{2}\delta_t \partial_\alpha \sum_i c_{i\alpha} c_{iy} F_i - \frac{1}{2}\delta_t \partial_{t_0}\sum_i c_{iy} F_i, \tag{A.14}$$

where the second order moment of F_i, $\sum_i c_{i\alpha} c_{iy} F_i$, can be calculated as $c_s^2 A\delta_{\alpha y} + \frac{1}{2}(C_{\alpha y} + C_{y\alpha})$, according to Guo *et al* in [14]. Using property (A.5), equation (A.14) can be simplified as:

$$\partial_{t_1}(\rho u_y) = \delta_t \left(m - \frac{n}{2}\right)\partial_{t_0} F_y + \partial_\alpha \sigma'_{\alpha y}, \tag{A.15}$$

where the viscous stress tensor $\sigma'_{\alpha y}$ is given by:

$$\sigma'_{\alpha y} = -\left(1 - \frac{\lambda_3}{2}\right)\Pi^{(1)}_{\alpha y} - \frac{\delta_t}{4}(C_{\alpha y} + C_{y\alpha}) - \frac{\delta_t}{6} A\delta_{\alpha y}, \tag{A.16}$$

and where $\Pi^{(1)}_{\alpha\beta}$ represents the 1st order momentum flux. In equation (A.15), the first term on the right hand side is eliminated by our previous choice of $n = 1$, $m = \frac{1}{2}$. Equation (A.15) is the MRT equivalence of equation (13b) in [14]. The assignment of $m = \frac{1}{2}$ accords with Guo *et al* but, interestingly, the constraint imposed by these authors $\left(n + \frac{m}{\tau}\right) = 1$ does not arise in the case of MRT dynamics.

Taking the second moment of equation (A.8) (i.e. multiplying by $c_{i\alpha} c_{i\beta}$ and summing on i), the re-arranging for $\Pi^{(1)}_{\alpha\beta}$ gives, after a fair amount of algebra outline shortly:

$$\frac{\Pi^{(1)}_{\alpha\beta}}{\delta_t} = -\frac{2\rho}{3\lambda_3} S_{\alpha\beta} - \frac{u_\alpha}{\lambda_3}(F_\beta - \partial_\beta \Phi') - \frac{u_\beta}{\lambda_3}(F_\alpha - \partial_\alpha \Phi')$$
$$+ \frac{1}{\lambda_3}\left[u_\gamma \partial_\gamma \Phi' - \frac{1}{3}\rho \partial_\gamma u_\gamma\right]\delta_{\alpha\beta}$$
$$+ \frac{1}{2\lambda_3}(C_{\alpha\beta} + C_{\alpha\beta}) + \frac{c_s^2}{\lambda_3} A\delta_{\alpha\beta} + \frac{1}{2\lambda_3} u_\alpha u_\beta A \tag{A.17}$$

where $S_{\alpha\beta} = \frac{1}{2}(\partial_\alpha u_\beta + \partial_\beta u_\alpha)$, and we have defined:

$$\Phi' = \frac{3}{5}(1-\alpha_R)(\rho_R + \Lambda\rho_B) - \frac{1}{3}\rho.$$

To obtain the expression for $\Pi^{(1)}_{\alpha\beta}$ in equation (A.17), we have used the definition of $f_i^{(0)}$ (see equations (2)) and (A.5) to introduce eigenvalue λ_3 and, crucially, we have used equation (A.9), which derives from a study of the model kinematics, to eliminate terms such as $\frac{\partial}{\partial t_1}(2\phi_1 + 4\phi_2)$ [24]. That is, the form of $\Pi^{(1)}_{\alpha\beta}$ given in equation (A.17) relies explicitly on the fact that ρ^N is a material invariant on the shortest timescales of the model.

Using the definition of the viscous stress tensor, equations (A.16) and (A.17), and simplifying, we obtain, after some algebra:

$$\begin{aligned}\frac{\sigma'_{\alpha\beta}}{\delta_t} = &-\frac{1}{2\lambda_3}\left(C_{\alpha\beta} + C_{\beta\alpha}\right) + \frac{2}{3}\left(\frac{1}{\lambda_3} - \frac{1}{2}\right)\rho S_{\alpha\beta} \\ &+ \left(\frac{1}{\lambda_3} - \frac{1}{2}\right)\left[u_\alpha\left(F_\beta - \partial_\beta\Phi'\right) + u_\beta\left(F_\alpha - \partial_\alpha\Phi'\right)\right] \\ &- \left(\frac{1}{\lambda_3} - \frac{1}{2}\right)\left[u_\gamma\partial_\gamma\Phi' - \frac{1}{3}\rho\partial_\gamma u_\gamma\right]\delta_{\alpha\beta} \\ &- \frac{1}{3\lambda_3}A\delta_{\alpha\beta} - \left(\frac{1}{\lambda_3} - \frac{1}{2}\right)Au_\alpha u_\beta. \end{aligned} \tag{A.18}$$

The discrepancy between the desired result (a term in $\rho S_{\alpha\beta}$) and equation (A.18) defines the error term to be eliminated:

$$\begin{aligned}E_{\alpha\beta} = &-\frac{1}{2\lambda_3}\left(C_{\alpha\beta} + C_{\beta\alpha}\right) \\ &+ \left(\frac{1}{\lambda_3} - \frac{1}{2}\right)\left[u_\alpha\left(F_\beta - \partial_\beta\Phi'\right) + u_\beta\left(F_\alpha - \partial_\alpha\Phi'\right)\right] \\ &- \left(\frac{1}{\lambda_3} - \frac{1}{2}\right)\left[u_\gamma\partial_\gamma\Phi' - \frac{1}{3}\rho\partial_\gamma u_\gamma\right]\delta_{\alpha\beta} \\ &- \frac{1}{3\lambda_3}A\delta_{\alpha\beta} - \left(\frac{1}{\lambda_3} - \frac{1}{2}\right)Au_\alpha u_\beta. \end{aligned} \tag{A.19}$$

Therefore, we make the following choice for tensor $C_{\alpha\beta}$ in our kinetic scale evolution equation, to correct the macro-scale dynamics

$$\begin{aligned}C_{\alpha\beta} = &\left(1 - \frac{\lambda_3}{2}\right)\left[u_\alpha\left(F_\beta - \partial_\beta\Phi'\right) + u_\beta\left(F_\alpha - \partial_\alpha\Phi'\right)\right] \\ &- \left(1 - \frac{\lambda_3}{2}\right)\left[u_\gamma\partial_\gamma\Phi' - \frac{1}{3}\rho\partial_\gamma u_\gamma\right]\delta_{\alpha\beta} \\ &- \left(1 - \frac{\lambda_3}{2}\right)Au_\alpha u_\beta - \frac{A}{3}\delta_{\alpha\beta}. \end{aligned} \tag{A.20}$$

With this choice of $C_{\alpha\beta}$, we obtain from equation (A.18) for the model viscous stress $\sigma_{\alpha\beta} = \frac{2}{3}\left(\frac{1}{\lambda_3} - \frac{1}{2}\right)\rho S_{\alpha\beta}\delta_t$, whereupon it is immediate that the kinematic viscosity is given by

$$\nu = \frac{1}{6}\left(\frac{2}{\lambda_3} - 1\right).$$

The source term F_i in equation (A.1) may now be conveniently partitioned into: (i) a term responsible for correcting the model dynamics in the presence of density gradients associated with component changes, (ii) a term responsible for the Lishchuk force and (iii) a term resulting from the continuity equation not equalling to zero:

$$F_i = F_{1i} + F_{2i} + F_{3i}, \tag{A.21}$$

where:

$$\begin{aligned} F_{1i} =& \frac{t_i}{2c_s^4}\left(1-\frac{\lambda_3}{2}\right)\left\{\frac{1}{3}\rho\partial_\gamma u_\gamma \delta_{\alpha\beta}\right. \\ &\left. -\left(u_\alpha\partial_\beta\Phi' + u_\beta\partial_\alpha\Phi' + u_\gamma\partial_\gamma\Phi'\delta_{\alpha\beta}\right)\right\}(c_{i\alpha}c_{i\beta} - c_s^2\delta_{\alpha\beta}), \end{aligned} \tag{A.22}$$

$$F_{2i} = t_i\left\{\frac{F_\alpha c_{i\alpha}}{c_s^2} + \frac{1}{2c_s^4}\left(1-\frac{\lambda_3}{2}\right)(u_\alpha F_{\beta_1} + u_\beta F_{\alpha_1})(c_{i\alpha}c_{i\beta} - c_s^2\delta_{\alpha\beta})\right\} \tag{A.23}$$

and

$$F_{3i} = t_i A - \left(1-\frac{\lambda_3}{2}\right)Au_\alpha u_\beta - \frac{1}{3}A\delta_{\alpha\beta}.$$

From equations (20) and (A.22) we identify:

$$\begin{aligned} F_{\alpha\beta} =& \frac{1}{2c_s^4}\left(1-\frac{\lambda_3}{2}\right)\left\{\frac{1}{3}\rho\partial_\gamma u_\gamma\delta_{\alpha\beta}\right. \\ &\left. -\left(u_\alpha\partial_\beta\Phi' + u_\beta\partial_\alpha\Phi' + u_\gamma\partial_\gamma\Phi'\delta_{\alpha\beta}\right)\right\}. \end{aligned}$$

The development of an MRT scheme for MCLBE after Dellar *et al* now reduces to one of recasting the model in terms of a set of linearly-dependent modes (defined in table 1). This process is described in section 3.2. The particular modal equations, determined from equation (1) and table 1 are the following 'forced' modal evolution equations of simple, scalar relaxation:

$$i = 0: \quad \rho^+ = \rho + A, \tag{A.24}$$

$$i = 1: \quad (\rho u_x)^+ = \rho u_x + nF_x\delta_t, \tag{A.25}$$

$$i = 2: \quad (\rho u_y)^+ = \rho u_y + nF_y\delta_t, \tag{A.26}$$

$$i = 3: \quad (P_{xx})^+ = P_{xx} - \lambda_3\left(P_{xx} - \Pi_{xx}^{(0)}\right) + \frac{\delta_t}{2}(C_{xx} + C_{xx}) + \frac{1}{3}A, \tag{A.27}$$

$$i = 4: \quad (P_{yy})^+ = P_{yy} - \lambda_3\left(P_{yy} - \Pi_{yy}^{(0)}\right) + \frac{\delta_t}{2}(C_{yy} + C_{yy}) + \frac{1}{3}A, \tag{A.28}$$

$$i = 5: \quad (P_{xy})^+ = P_{xy} - \lambda_3\left(P_{xy} - \Pi_{xy}^{(0)}\right) + \frac{\delta_t}{2}(C_{xy} + C_{yx}), \tag{A.29}$$

$$i = 6: \quad N^+ = N - \lambda_6 N, \tag{A.30}$$

$$i = 7,\ 8: \quad J_\alpha^+ = J_\alpha - \lambda_7 J_\alpha, \tag{A.31}$$

where $\alpha \in [x, y]$. We note the simple form of the relaxation equations for $\mathbf{h}^{(6)}, \cdots, \mathbf{h}^{(8)}$, i.e. N, J_x, J_y, which for $\lambda_6 = \lambda_7 = 1$, reduce to $N^+ = J_x^+ = J_y^+ = 0$. This is a direct consequence of the choice of equilibria. Note that the fact that the scheme devised contains source and sinks is apparent from the first of the above modal equations.

Appendix B. High order lattice stencils

It is possible to exploit lattice tensor isotropy, to develop non-compact stencils of any chosen order of accuracy for first gradient quantities. Thampi *et al* have given a similar treatment of this essential approach [30] but based around the other gradient quantities (the Laplacian).

Consider a scalar function denoted f. No confusion with the colour-blind distribution function, f_i, should arise from use of this notation. A multi-variate Taylor expansion, on the lattice, of function $f(\mathbf{r})$ may be written: $f(\mathbf{r} + N\mathbf{c}_i) = f(\mathbf{r}) + \sum_{n=1}^{\infty} \frac{N^n}{n!} (\mathbf{c} \cdot \nabla)^n f$. Taking moments of this expansion with $t_i c_{ix}$ and appealing to lattice properties (A.6), we straightforwardly obtain:

$$\sum_i t_i f(\mathbf{r} + N\mathbf{c}_i) c_{ix} = \frac{N}{3} \frac{\partial f}{\partial x} + \sum_{n=2}^{\infty} \frac{N^{(2n-1)}}{(2n-1)!} E_{(2n-1)}, \tag{B.1}$$

where $N \in \mathbb{Z}^+$, and we define the mth error term:

$$E_m = \left(\sum_{i=1}^{Q} t_i c_{ix} c_{i\alpha_1} c_{i\alpha_2} .. c_{i\alpha_m} \right) \left(\frac{\partial^m f}{\partial x_{\alpha_1} \partial x_{\alpha_2} ... \partial x_{\alpha_m}} \right). \tag{B.2}$$

We need not be concerned with expressions for the E_m to eliminate them.

Let us obtain a non-compact stencil for $\frac{\partial f}{\partial x}$, correct to (say) fifth order, using straightforward linear algebra methods. Take $N \in [1..3]$ in equation (B.1) and truncate each equation at $n > 3$, to obtain three equations (one for each choice of N). These three equations may be written as follows, in matrix form:

$$\begin{bmatrix} \sum_i t_i f(\mathbf{r} + \mathbf{c}_i) c_{ix} \\ \sum_i t_i f(\mathbf{r} + 2\mathbf{c}_i) c_{ix} \\ \sum_i t_i f(\mathbf{r} + 3\mathbf{c}_i) c_{ix} \end{bmatrix} = \begin{bmatrix} \frac{1^1}{1!} & \frac{1^3}{3!} & \frac{1^5}{5!} \\ \frac{2^1}{1!} & \frac{2^3}{3!} & \frac{2^5}{5!} \\ \frac{3^1}{1!} & \frac{3^3}{3!} & \frac{3^5}{5!} \end{bmatrix} \begin{bmatrix} \frac{1}{3} \frac{\partial f}{\partial x} \\ E_{(3)} \\ E_{(5)} \end{bmatrix}. \tag{B.3}$$

The inverse matrix of co-efficients, $C_{ij} = \frac{i^{(2j-1)}}{(2j-1)!}$ exists and may be computed. Inverting the above, then, we find an expression for $\frac{\partial f}{\partial x}$ as:

$$\frac{\partial f}{\partial x} = \begin{bmatrix} \frac{9}{2} & -\frac{9}{10} & \frac{1}{10} \end{bmatrix} \begin{bmatrix} \sum_i t_i f(\mathbf{r} + \mathbf{c}_i) c_{ix} \\ \sum_i t_i f(\mathbf{r} + 2\mathbf{c}_i) c_{ix} \\ \sum_i t_i f(\mathbf{r} + 3\mathbf{c}_i) c_{ix}. \end{bmatrix} \tag{B.4}$$

Clearly, this approach may be adapted to yield expressions for gradients of chosen accuracy.

ORCID iDs

X Xu https://orcid.org/0000-0002-9721-9054
M Seaton https://orcid.org/0000-0002-4708-573X
I Halliday https://orcid.org/0000-0003-1840-6132

References

[1] Gunstensen A K, Rothman D H, Zaleski S and Zanetti G 1991 *Phys. Rev.* A **43** 4320
[2] Rothman D H and Keller J M 1988 *J. Stat. Phys.* **52** 1119
[3] Rothman D H and Zaleski S 1994 *Lattice Gas Cellular Automata, Collection Ala-Saclay* (Cambridge: Cambridge University Press)
[4] Swift M R, Osborn W R and Yeomans J M 1995 *Phys. Rev. Lett.* **75** 830
[5] Swift M R, Orlandini E, Osborn W R and Yeomans J M 1996 *Phys. Rev.* E **54** 5041
[6] Wagner A J 2006 *Phys. Rev.* E **74** 056703
[7] Li Q and Wagner A J 2007 *Phys. Rev.* E **76** 036701
[8] Wagner A J and Pooley C M 2007 *Phys. Rev.* E **76** 056703
[9] Shan X and Chen H 1994 *Phys. Rev.* E **49** 2941
[10] Landau L and Lifshitz E M 1966 *Fluid Mechanics* 6th edn (Oxford: Pergamon)
[11] Lishchuk S V, Care C M and Halliday I 2003 *Phys. Rev.* E **67** 036701
[12] D'Ortona U, Salin D, Cieplak M, Rybka R B and Banavar J R 1995 *Phys. Rev.* E **51** 3718
[13] Peskin C S 2002 *Acta Numer.* **11** 479
[14] Guo Z, Zheng C and Shi B 2002 *Phys. Rev.* E **65** 046308
[15] Halliday I, Hollis A P and Care C M 2007 *Phys. Rev.* E **76** 026708
[16] Reiss T and Phillips T N 2007 *J. Phys. A: Math. Gen.* **40** 4033
[17] Ba Y, Liu H, Li Q, Kang Q and Sun J 2016 *Phys. Rev.* E **94** 023310
[18] Qian Y H, d'Humières D and Lallemand P 1992 *Europhys. Lett.* **17** 479
[19] Liu H, Valocchi A J and Kang Q 2012 *Phys. Rev.* E **85** 046309
[20] Wen Z X, Li Q, Yu Y and Luo K H 2019 *Phys. Rev.* E **100** 023301
[21] Spendlove J, Xu X, Halliday O J, Schenkel T and Halliday I 2019 *Phys. Rev.* E under review
[22] Halliday I, Xu X and Burgin K 2017 *Phys. Rev.* E **95** 023301
[23] Xu X, Burgin K, Ellis M A and Halliday I 2017 *Phys. Rev.* E **96** 053308
[24] Burgin K, Spendlove J, Xu X and Halliday I 2019 *Phys. Rev.* E **100** 043310
[25] Dellar P J 2002 *Phys. Rev.* E **65** 036309
[26] Hou S, Zou Q, Chen S, Doolen G and Cogley A C 1995 *J. Comput. Phys.* **118** 329
[27] Benzi R, Succi S and Vergassola M 1992 *Phys. Rep.* **222** 145
[28] Benzi R, Succi S and Vergassola M 1990 *Europhys. Lett.* **13** 727
[29] Arfken G 1970 *Mathematical Methods for Physicists* 2nd edn (New York: Academic)
[30] Thampi S P, Ansumali S, Adhikari R and Succi S 2013 *J. Comput. Phys.* **234** 1
[31] Rybczynski W 1911 *Bull. Acad. Sci. Cracovie* A **40** 46
[32] Hadamard J S 1911 *Comput. Rend. Acad. Sci.* **152** 1735
Hadamard J S 1912 *Comput. Rend. Acad. Sci.* **154** 109
[33] Happel J and Brenner H 1973 *Low Reynolds Number Hydrodynamics* (Leyden: Noordhoff International Publishing)
[34] Taylor T D and Acrivos A 1964 *J. Fluid Mech.* **18** 466
[35] Halliday I, Lishchuk S V, Spencer T J, Burgin K and Schenkel T 2017 *Comput. Phys. Commun.* **219** 286
[36] Guo Z and Zhao T S 2002 *Phys. Rev.* E **66** 036304
[37] Inamuro T *et al* 2004 *J. Comput. Phys.* **198** 628